communications biology

A Nature Portfolio journal

Article

https://doi.org/10.1038/s42003-026-09801-w

Dual targeting of topoisomerase I and DNA G-quadruplexes enhances senescence and chemosensitivity in colorectal cancer

Yameng Li[1,2], Donglei Ji[1], Yanjie Jia[1], Yingying Liang[1,2], Enwei Wei[1,2], Chunfeng Gao[1,2], Yongqi Li[3], Caroline Zeng[4], Liping Wang[1,2], Chunyu Wang[5], Zhen Guo[6], Yiqun Zhang[6], Ming-Ming Zhou[7] ✉, Di Wu[6] ✉ & Lei Zeng[1,2] ✉

Colorectal cancer (CRC) remains a therapeutic challenge due to chemoresistance that limits conventional treatment efficacy. We developed ZBH-01, a camptothecin derivative engineered to target both topoisomerase I (TOP1) and DNA G-quadruplexes (G4s). Unlike irinotecan (CPT-11), which requires metabolic activation, ZBH-01 directly stabilizes TOP1-DNA covalent complexes and preferentially binds the *hTERT* promoter G4, a regulator of telomere maintenance and oncogenic transcription. Structural studies reveal that the crescent-shaped scaffold of ZBH-01 π-π stacks onto the external G-tetrad of the *hTERT* G4, displacing SP1/MYC transcription factors and suppressing hTERT expression. Functionally, ZBH-01 demonstrated improved efficacy in chemoresistant models, exhibiting 14-fold and 7-fold greater efficacy than CPT-11 and SN-38 respectively in cisplatin-resistant cells, and outperforming CPT-11 by 61-fold and SN-38 by 2.4-fold in 5-FU-resistant models. By concurrently disrupting DNA repair through TOP1-trapping and transcriptional adaptation via G4-stabilization, ZBH-01 induced DNA damage, telomere shortening, and cellular senescence. These findings establish TOP1/G4 dual-targeting as a potential therapeutic strategy to enhance CRC chemosensitivity, presenting a new framework for combining DNA damage induction with transcription modulation.

Colorectal cancer (CRC) ranks as the third most lethal malignancy worldwide[1,2]. It remains a formidable clinical challenge due to tumor heterogeneity and chemoresistance[3,4]. Despite advancements in therapeutic strategies such as 5-fluorouracil (5-FU), cisplatin (DDP), irinotecan (CPT-11), and targeted biologics (e.g., bevacizumab, cetuximab)[5–10], treatment efficacy remains limited by adaptive resistance mechanisms. These limitations highlight the need for innovative strategies that simultaneously disrupt complementary oncogenic pathways, targeting both genomic stability and transcriptional regulation to impair cancer survival.

Topoisomerase I (TOP1) is a nuclear enzyme critical for DNA supercoiling resolution during replication and transcription[11]. It represents a well-established therapeutic target inhibited by the camptothecin derivative CPT-11[12]. However, CPT-11's clinical efficacy is constrained by its dependence on enzymatic conversion to the active metabolite SN-38 (7-ethyl-10-hydroxycamptothecin)[13–15]. This process achieves only 2–8% efficiency in vivo[16,17]. Although SN-38 demonstrates potent TOP1 inhibition (100- to 1000-fold greater than CPT-11) through stabilization of TOP1-DNA covalent complexes[18], its therapeutic potential is suffered by rapid glucuronidation[19], poor aqueous solubility, and dose-limiting toxicity[18–20]. These pharmacokinetic and pharmacodynamic challenges underscore the need for developing structurally optimized camptothecin analogs that bypass metabolic activation while potentially engaging complementary oncogenic pathways, such as DNA G-quadruplex (G4) stabilization.

DNA G-quadruplexes (G4s) are promising therapeutic targets as their non-canonical secondary structures highly enriched in oncogene promoters (e.g., *hTERT*, *MYC*, *KRAS*) and telomeres[21]. Computational studies predict over 370,000 G4 motifs genome-wide[22], with preferential

[1]Institute of Translational Medicine, The First Hospital of Jilin University, Changchun, China. [2]International Center of Future Science, Jilin University, Changchun, China. [3]Institute of Liver Diseases, The First Hospital of Jilin University, Changchun, China. [4]Pennsylvania State University College of Medicine, Hershey, PA, USA. [5]State Key Laboratory of Supramolecular Structure and Materials, College of Chemistry, Jilin University, Changchun, China. [6]Department of Cancer Centre, The First Hospital of Jilin University, Changchun, China. [7]Department of Pharmacological Sciences, Icahn School of Medicine at Mount Sinai, New York, NY, USA. ✉e-mail: ming-ming.zhou@mssm.edu; wudi1971@jlu.edu.cn; leizeng@jlu.edu.cn

localization in cancer-associated genes where they regulate transcription[23]. Pharmacological stabilization of G4s disrupts transcription, replication, and telomere maintenance[24]. However, despite decades of research and development of more than 5000 synthetic G4-targeting ligands (e.g., porphyrins, acridines)[25–27], clinical translation remains challenged by poor pharmacokinetics and ambiguous structural effects. We propose a dual-targeting strategy integrating G4 stabilization with TOP1 inhibition to address limitations of single-mechanism therapies. This combined approach aims to promote replication-associated DNA damage via TOP1-DNA trapping while epigenetically silencing oncogenic drivers like *hTERT* through G4-mediated transcriptional suppression.

Human telomerase reverse transcriptase (hTERT) is the catalytic subunit of telomerase. It is aberrantly overexpressed in over 85% of cancers to sustain proliferation and evade senescence[28,29]. The *hTERT* promoter contains conserved DNA G4 motifs that regulate telomerase expression[30,31]. Pharmacological G4 stabilization suppresses hTERT expression, inducing telomere shortening, senescence and apoptosis[32]. Here, we introduce ZBH-01, a camptothecin derivative engineered to concurrently inhibit TOP1 and stabilize oncogenic G4 structures. Unlike single-mechanism agents (CPT-11, SN-38, TMPyP4)[33], ZBH-01 integrates two therapeutic modalities: (1) TOP1 inhibition inducing replication-associated DNA damage, and (2) G4-driven epigenetic suppression. NMR structural studies reveal that the crescent-shaped scaffold of ZBH-01 stacks onto the 3'-terminal G-tetrad of the *hTERT* G4, displacing oncogenic transcription factors SP1 and MYC while stabilizing TOP1-DNA complexes. This dual mechanism enables enhanced therapeutic effects through coordinated genomic and epigenetic disruption, inducing DNA damage (γ-H2AX), telomere shortening, and senescence in CRC cells. ZBH-01 demonstrates superior potency in cisplatin- and 5-FU-resistant CRC models, outperforming single-target agents and supporting an approach that merges DNA damage induction (via TOP1 trapping) with epigenetic modulation (via G4 stabilization) for overcoming treatment resistance in colorectal cancer.

Results

ZBH-01 binds to the TOP1-DNA covalent complex and inhibits cell proliferation

We developed ZBH-01, a newly synthesized camptothecin derivative engineered through structure-based optimization to enhance TOP1 inhibition and aqueous solubility[34]. The compound incorporates an N-methylpiperazine moiety to improve solubility via salt formation and an N-formylglycine linker to modulate TOP1-binding affinity (Fig. 1A, Supplementary Fig. 1A). Quantitative solubility testing confirmed that ZBH-01 achieved exceptional solubility (0.65–15.8 mg/mL in PBS) (Supplementary Fig. 1B, C), representing a >2600-fold improvement over SN-38 (<0.25 μg/mL)[35], while maintaining stability in vitro (Supplementary Fig. 1D, E).

Subsequent biophysical screening unexpectedly revealed that these structural modifications also enabled G-quadruplex (G4) stabilization, uncovering a dual-targeting mechanism. In anti-proliferative assays across eight cancer cell lines (LS174T, HCT116, HCT8, SW480, A549, HeLa, MCF7, and PC3), ZBH-01 reduced cellular viability with potency equivalent to SN-38 and significantly outperformed CPT-11 (Fig. 1B, Supplementary Fig. 2). Unlike CPT-11, which requires inefficient metabolic activation, ZBH-01 showed direct cytotoxicity across cell lines (Fig. 1B), highlighting its broad efficacy across cancer types and the potential to address pharmacokinetic limitations. The reduced efficacy in SW480 cells may reflect low expression of key targets (*hTERT*, *TOP1*, *MYC*)[36], potentially impairing dual-mechanism engagement.

An immunocomplex of enzyme (ICE) assay confirmed ZBH-01's direct engagement with TOP1-DNA complexes. Slot-blotting analysis of fractions 2–5 revealed that ZBH-01 and SN-38 robustly stabilized endogenous TOP1-DNA complexes, with ZBH-01 showing superior effects compared to CPT-11 (Fig. 1C). To understand molecular interactions of ZBH-01, we performed molecular docking analysis of the binding mode of ZBH-01 within the TOP1-DNA cleavage site (PDB ID: 1T8I)[37]. ZBH-01, SN-38 and camptothecin (CPT) all adopt similar planar orientations stabilized by π-π stacking with DNA base pairs (Cyt112-Gua11 and Ade113-Thy10) (Fig. 1D–F). All three compounds formed characteristic interactions with TOP1 residues, including hydrogen bonds with Asp533 and Thr718, hydrophobic contacts, and a salt bridge with Arg364 (Fig. 1D–F)[37]. Notably, the *N*-methylpiperazine and *N*-Formylglycine moieties of ZBH-01 established additional interactions with TOP1 residues (Ala351, Asn352, Glu356, Trp416, Lys425, Tyr426, Met428) (Fig. 1D), while SN-38 forms an additional hydrogen bond with Glu356 (Fig. 1E). In contrast, the bulky bis-piperidines moiety of CPT-11 sterically hindered optimal interaction with the DNA cleavage site, explaining its reduced efficacy in stabilizing TOP1-DNA complexes. These structural insights provide a molecular rationale for ZBH-01's enhanced TOP1 inhibitory activity compared to existing camptothecin analogs.

To explore the mechanisms underlying ZBH-01-induced TOP1 downregulation through proteasomal and SUMOylation pathways, we treated LS174T and HCT116 cells with ZBH-01, SN-38, or CPT-11 in the presence or absence of pathway-specific inhibitors targeting the proteasome (MG132), SUMOylation (ML-792), or autophagy (chloroquine). Treatment with ZBH-01 or SN-38 reduced TOP1 protein levels, while CPT-11 showed minimal effect (Fig. 1G and Supplementary Fig. 3A–C), consistent with the direct TOP1-targeting activity of ZBH-01 inherited from its camptothecin core. Notably, MG132 and ML-792 partially rescued TOP1 levels, whereas chloroquine had no effect. (Fig. 1G and Supplementary Fig. 3A–C), indicating ubiquitin-proteasome and SUMOylation pathways involved in TOP1 regulation. Intriguingly, MG132 was less effective in reversing ZBH-01-induced degradation compared to SN-38 (Fig. 1G), suggesting that ZBH-01 engages additional regulatory mechanisms beyond canonical proteasomal degradation.

ZBH-01 activates cellular senescence in CRC cells

To investigate genome-wide transcriptional effect by the dual-targeting mechanism of ZBH-01, we performed RNA sequencing (RNA-seq) on LS174T cells treated with ZBH-01, CPT-11, or SN-38. ZBH-01 induced substantial transcriptomic alterations, downregulating 2,872 genes and upregulating 2,758 genes (fold change > 1.2, $p < 0.05$; Supplementary Fig. 4A). This effect was moderately higher than SN-38 (2,638 downregulated, 2,607 upregulated) but markedly exceeded CPT-11 (284 downregulated, 574 upregulated; Supplementary Fig. 4B, C), demonstrating its broad transcriptional influence.

Kyoto Encyclopedia of Genes and Genomes (KEGG) pathway and Gene Ontology (GO) enrichment analyses identified significant enrichment in cancer-related processes, including cellular senescence, DNA replication, cell cycle regulation, DNA damage response, and telomere maintenance (Fig. 2A, B). Notably, RNA-seq profiling revealed *hTERT* and *MYC*, critical senescence regulators with G4-rich promoters, among the most significantly downregulated genes (Fig. 2C and Supplementary Fig. 4D). This transcriptional repression was validated by RT-qPCR showing reduced mRNA levels of cell cycle drivers (*CCNB1*, *CCNB2*, *CCNA2*, *CDC25A*) and senescence regulators (*FOXM1*, *MYBL2*, *CHEK1*, *hTERT*, *MYC*) (Fig. 2D). Western blot analysis confirmed corresponding protein reduction of Cyclin A2 (encoded by *CCNA2*), MYBL2, hTERT, and MYC (Fig. 2E). The more pronounced reduction in Cyclin A2 protein (91%; Fig. 2E) compared to its mRNA (66–68% reduction) (Fig. 2D) suggests the possibility of accelerated proteasomal degradation (half-life ~20 min)[38], consistent with ZBH-01's multi-layer disruption of cell cycle regulation.

To elucidate the molecular network of ZBH-01-responsive genes, we conducted protein-protein interaction (PPI) network analysis using the STRING database. We identified a tightly interconnected network of 41 genes (Fig. 2F). Among these, eight hub genes emerged as central senescence regulators, including *CALM3, MAPK14, CDK2, CDK4, CHEK1*, *TERT*, *KRAS* and *MYC* (Fig. 2F, highlighted in yellow). TCGA-COAD data analysis demonstrated significant overexpression of most hub genes (*MAPK14, CDK2, CDK4, CHEK1*, *TERT*, and *MYC*) in CRC tumors compared to normal tissues, whereas *KRAS* and *CALM3* were downregulated (Fig. 2G and Supplementary Fig. 4E). Clinically, only *hTERT* expression strongly

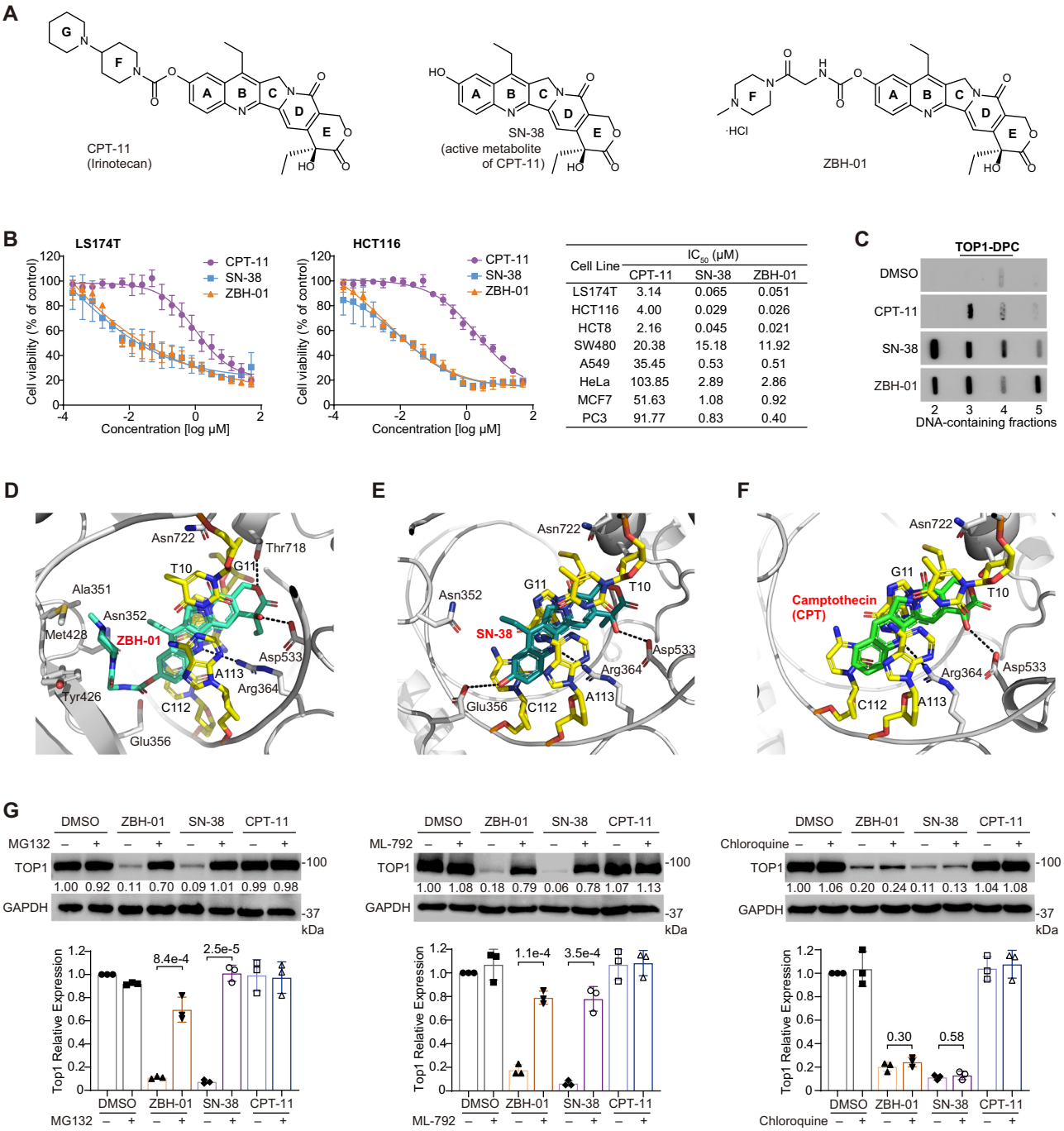

Fig. 1 | ZBH-01 suppresses cell proliferation, stabilizes TOP1-DNA complexes, and induces TOP1 degradation via SUMOylation/proteasome pathways. **A** Chemical structures of topoisomerase I (TOP1) inhibitors CPT-11, SN-38 and ZBH-01. **B** Inhibition of cell viability by ZBH-01, CPT-11, and SN-38 across multiple cancer cell lines (MTT assay). Data represent mean ± SEM from at least three independent experiments. IC_{50} values were determined using IBM SPSS Statistics (Version 26). **C** Detection of TOP1-DNA covalent complexes in LS174T cells treated with ZBH-01, CPT-11, and SN-38 (4 μM, 0.5 h) by cesium chloride gradient centrifugation. Fractions (1–24) were collected from the bottom of the tubes, and TOP1 presence in each fraction was analyzed via western blotting with a TOP1 monoclonal antibody. Cellular DNA was enriched in fractions 2–5, corresponding to the TOP1-DNA complexes. Molecular docking models of ZBH-01 (**D**) or SN-38 (**E**) bound to the TOP1-DNA cleavage site (PDB ID: 1T8I). Key TOP1 residues are labeled in light-gray, DNA elements in yellow, ligands in light-green (ZBH-01) or dark-green (SN-38). Putative hydrogen bonds are represented by black dashed lines. Oxygen atoms are in red and nitrogen atoms in blue. **F** Expanded view of key inter-molecular interactions between camptothecin (CPT) and the TOP1-DNA complex (PDB ID: 1T8I), colored as above. **G** LS174T cells were pretreated with MG132 (10 μM), chloroquine (10 μM), or ML-792 (10 μM) for 1 h, followed by DMSO, ZBH-01 (1 μM), SN-38 (1 μM), or CPT-11 (5 μM) for additional 8 h. Cell lysates were immunoblotted with the indicated antibodies (upper panel). Quantitative data (lower panel) represent mean ± S.D. from at least three independent experiments. *p*-values for each comparison were derived from a two-tailed unpaired Student's *t*-test. Relative expression levels were normalized to GAPDH.

correlated with reduced overall survival (HR = 1.49, $p = 0.047$) and progression-free interval (HR = 1.51, $p = 0.025$) (Fig. 2H and Supplementary Fig. 4F). In contrast, *KRAS* expression showed limited association with overall survival only, and *MYC* exhibited no significant survival correlation (Supplementary Fig. 4F), indicating the distinct roles of these regulators in CRC pathogenesis. Notably, promoter regions of *hTERT, KRAS*, and *MYC* all contain DNA-G4 motifs[39–41], suggesting that ZBH-01-driven G4 stabilization mediates their transcriptional repression.

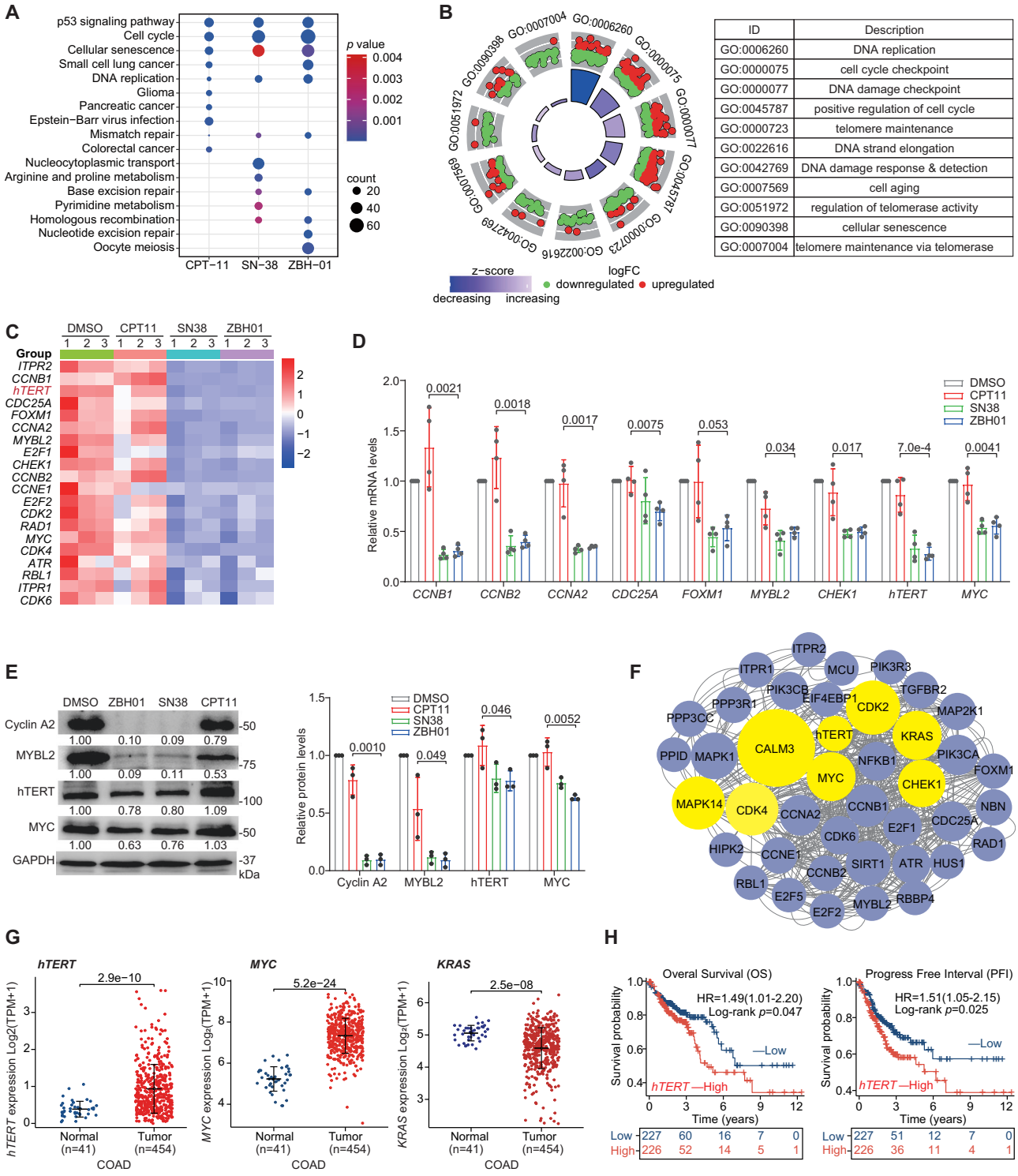

Fig. 2 | ZBH-01 activates cellular senescence pathways in CRC cells. A KEGG signaling pathway enrichment analysis of up- and down-regulated genes in LS174T cells treated with ZBH-01, CPT-11, or SN-38. Only the top 10 enriched signaling pathways are shown. **B** Gene Ontology Biological Process (GO-BP) analysis of differentially expressed genes in ZBH-01-treated LS174T cells, displaying the top 10 GO terms. **C** Heatmap of differentially expressed cellular senescence-related genes in LS174T cells treated with DMSO (control), CPT-11, SN-38, or ZBH-01. Only the top 20 down-regulated genes following ZBH-01 treatment are shown. **D** RT-qPCR analysis of cellular senescence-related genes and genes containing G4 structures after treatment with DMSO, ZBH-01 (100 nM), SN-38 (100 nM), or CPT-11 (500 nM) for 24 h in LS174T cells. Data are presented as mean ± S.D. ($n \geq 4$ independent experiments per condition). *p*-values for each comparison were determined using a two-tailed unpaired Student's *t*-test. **E** Western blot analysis of CCNA2, MYBL2, hTERT, and MYC protein levels in LS174T cells treated with DMSO, ZBH-01 (100 nM), SN-38 (100 nM), CPT-11 (500 nM) for 48 h. Quantitative data are shown as mean ± S.D. ($n \geq 3$ independent experiments per condition). *p*-values were calculated using a two-tailed unpaired Student's *t*-test. Relative protein expression was normalized to GAPDH. **F** Protein-protein interaction (PPI) network of down-regulated cellular senescence genes in ZBH-01-treated LS174T cells. The PPI network was exported from STRING and visualized in Cytoscape. **G** Comparison of hTERT, MYC, and KRAS expression between colorectal cancer tumors and normal tissues based on the TCGA database. **H** Kaplan-Meier analysis based on the TCGA data, evaluating the association between hTERT expression and patient overall survival and progression-free interval.

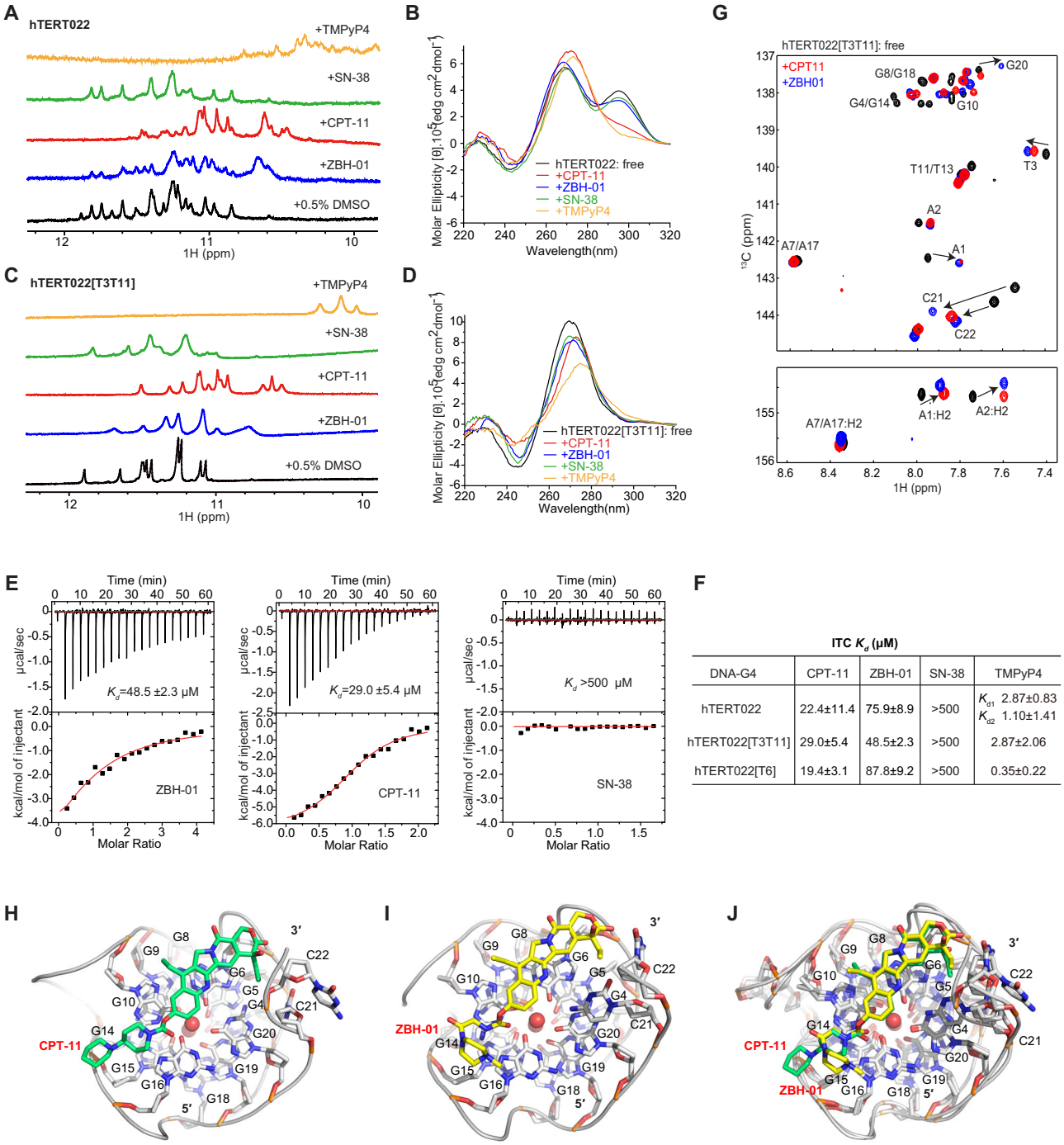

DNA-G4	CPT-11	ZBH-01	SN-38	TMPyP4
hTERT022	22.4±11.4	75.9±8.9	>500	K_{d1} 2.87±0.83 K_{d2} 1.10±1.41
hTERT022[T3T11]	29.0±5.4	48.5±2.3	>500	2.87±2.06
hTERT022[T6]	19.4±3.1	87.8±9.2	>500	0.35±0.22

Molecular details of ZBH-01 binding to the *hTERT* G4

To investigate the structural mechanism of the dual-targeting activity of ZBH-01, we performed NMR-based binding studies using seven promoter-derived G-rich DNA sequences (*hTERT*[30], *KIT*[42], *KRAS*[43], *MYC*[44], *BCL2*[45], *PARP1*[46] and *VEGF*[47]; Supplementary Table 1) under physiologically relevant potassium conditions (90 mM K^+). Characteristic imino proton peaks (10.5–12.0 ppm) in 1D ^{1}H-NMR spectra confirmed stable, three-layer folded G-quadruplex structures for all sequences (Fig. 3A and Supplementary Fig. 5A)[30]. Titration with ZBH-01, CPT-11 or the classical G4 ligand TMPyP4 induced significant chemical shift perturbations (CSPs) in the imino region[33], indicating direct binding, while SN-38 showed negligible effects (Fig. 3A and Supplementary Fig. 5A, B). Notably, ZBH-01 and CPT-11 exhibited stronger CSPs for *hTERT*, *KIT*, *KRAS*, and *VEGF* G4s compared to *MYC*, *BCL2* and *PARP1* (Fig. 3A and Supplementary Fig. 5A), indicating sequence-dependent binding affinity and structural selectivity toward specific G4 conformations.

To further elucidate the conformational dynamics, we performed comparative NMR and circular dichroism (CD) analyses using wild-type and mutant *hTERT* G4 sequences (Table 1)[30]. Wild-type hTERT022 adopted a dynamic equilibrium between parallel and (3 + 1) hybrid topologies under 90 mM K^+ conditions. This conformational heterogeneity was evidenced by dispersed imino proton peaks (10.5–12.0 ppm) and characteristic CD signatures: a positive peak at 260 nm (parallel) and a broad signal at 280–300 nm (hybrid) (Fig. 3A, B)[30]. Treatment with ZBH-01 and CPT-11 shifted this equilibrium toward parallel topology, as marked by increased CD signal at 260 nm and reduced intensity at 280–300 nm

Fig. 3 | Structural mechanism of *hTERT* G4-DNA in complex with ZBH-01. **A** Imino proton regions of 1D ^{1}H NMR spectra of hTERT G4 DNA (hTERT022, 0.15 mM) in the absence (black) or presence of ZBH-01 (blue), CPT-11 (red), SN-38 (green) or TMPyP4 (yellow). The G4-DNA/ligand molar ratio is 1:3. Spectra were recorded in 20 mM potassium phosphate (KPi), 70 mM KCl, and 10% D_2O at pH 7.0 and 25 °C (0.5% DMSO in NMR control panels). **B** Circular dichroism (CD) spectra of hTERT022 G4 DNA (5 μM) in its free form (black) and in complex with ZBH-01 (blue), CPT-11 (red), SN-38 (green) or TMPyP4 (yellow) at a 1:3 G4-DNA/ligand molar ratio. CD spectra were collected in 20 mM KPi, 70 mM KCl, pH 7.0 at 25 °C. **C** Imino proton NMR spectra of thymine-substituted hTERT022[T3T11] G4-DNA in its free form (black, 0.15 mM) or in complex with ZBH-01 (blue), CPT-11 (red), SN-38 (green) or TMPyP4 (yellow) at a 1:3 G4-DNA/ligand molar ratio. Spectra were recorded in 20 mM KPi, 70 mM KCl and 10% D_2O, pH 7.0 and 25°C (0.5% DMSO in NMR control panels). **D** CD spectra for hTERT022[T3T11] G4-DNA in its free state (black, 5 μM) or in complex with ZBH-01 (blue), CPT-11 (red), SN-38 (green) or TMPyP4 (yellow) at a 1:3 G4-DNA/ligand molar ratio. Samples were prepared in 20 mM KPi and 70 mM KCl, pH 7.0 at 25 °C. **E**, **F** Isothermal titration calorimetry (ITC) measurements of the binding affinities of ZBH-01, CPT-11, SN-38 or TMPyP4 to hTERT022, hTERT022[T3T11] and hTERT022[T6] G4-DNA. Solid lines represent nonlinear least squares fits using a single-site binding model. Data represent mean ± S.D. ($n \geq 3$ independent experiments). **G** Overlays of ^{1}H-^{13}C-HSQC NMR spectra of hTERT022[T3T11] G4-DNA in the absence (black) or presence of ZBH-01 (blue) or CPT-11 (red) at a 1:4 G4-DNA/ligand molar ratio. Peaks showing significant chemical shift perturbations are labeled with nucleotide numbers. Arrows indicate chemical shift changes for individual peaks. Data were collected at 25 °C in 20 mM KPi, 70 mM KCl, and 10% D_2O, pH 7.0 (0.5% DMSO in NMR control panels). Expanded views of key inter-molecular interactions between hTERT022[T3T11] G4-DNA and CPT-11 (**H**) or ZBH-01 (**I**). hTERT022[T3T11] nucleotides are shown in light-gray, CPT-11 in green, and ZBH-01 in yellow. Oxygen and potassium atoms are highlighted in red, and nitrogen atoms in blue. **J** Structural alignment of nucleotides involved in ligand binding between hTERT022[T3T11]/CPT-11 and hTERT022[T3T11]/ZBH-01 complexes. CPT-11 is shown in green, ZBH-01 in yellow, with selected nucleotides in the G4-DNA binding sites displayed as sticks, following the same color scheme as in (**H**, **I**).

Table 1 | Properties of Four-G-Tract Sequences Used in This Study

Name	Sequence[a]	Position[b]	Topology[c]
hTERT022	AAGGGGAGGGGCTGGGAGGGCC	−92	Parallel/(3 + 1) hybrid
hTERT022[T3T11]	AA**T**GGGAGGG**T**CTGGGAGGGCC		Parallel
hTERT022[T6]	AAGGG**T**AGGGGCTGGGAGGGCC		(3 + 1) hybrid

[a]Guanines constituting the four G-tracts are underlined. Substituted thymine (T) residues are shown in boldface.
[b]Position of the first nucleotide relative to the TSS site.
[c]The topology of the G-quadruplex (G4) structure formed by each sequence.

(Fig. 3B)[30]. Corresponding up-field shifts in NMR imino peaks further confirmed this conformational transition (Fig. 3A). This ligand-driven conformational stabilization was consistent with TMPyP4, and persisted even in thymine-mutated *hTERT* G4 structures hTERT022[T6] (native hybrid topology) and hTERT022[T3T11] (native parallel topology) (Fig. 3C, D, Supplementary Fig. 6A, B; Table 1), demonstrating that ZBH-01 and related compounds enforce a parallel G4 conformation regardless of initial structural preferences. These results indicate that ZBH-01 can selectively stabilize parallel G4 conformations through direct, sequence-dependent binding, providing a structural basis for its potential to modulate G4-mediated transcriptional regulation as part of its dual-targeting mechanism.

We next quantified ligand-G4 binding affinities using isothermal titration calorimetry (ITC). ITC results revealed distinct ligand-G4 binding profiles. ZBH-01 exhibited moderate G4-binding affinities for wild-type and mutant *hTERT* G4s (K_d = 48.5, 75.9, 87.8 μM), while CPT-11 showed 2–4-fold stronger binding (K_d = 19.4, 22.4, 29.0 μM) (Fig. 3E, F and Supplementary Fig. 6C). In contrast, TMPyP4 displayed sub-micromolar affinity (K_d = 0.35, 2.87, 2.87 μM), and SN-38 demonstrated negligible binding (K_d > 500 μM), confirming its inability to engage G4 structures (Fig. 3E, F and Supplementary Fig. 6C).

To define the structural basis of the dual-targeting activity of ZBH-01, we employed the stabilized parallel G4 mutant hTERT022[T3T11], which contains guanine-to-thymine substitutions at positions G3/G11. CD spectroscopy confirmed that ZBH-01 binding maintains the parallel topology, as evidenced by nearly identical spectra before and after treatment (Fig. 3D). NMR analysis revealed comparable CSPs in both wild-type hTERT022 and hTERT022[T3T11] mutant upon binding with ZBH-01, CPT-11 or TMPyP4 (Fig. 3A, C), indicating conserved ligand-G4 interactions despite the structural modification. Notably, the hTERT022[T3T11] mutant displayed enhanced NMR spectral resolution with sharper imino proton peaks, reflecting improved structural stability and reduced conformational heterogeneity compared to the wild-type G4. These findings establish hTERT022[T3T11] as a suitable model system for high-resolution structural studies of ligand-G4 interactions, while demonstrating that ZBH-01 achieves effective G4 engagement through moderate-affinity binding that preserves parallel G4 topology.

To elucidate the atomic-level basis of ZBH-01, we acquired 2D nuclear Overhauser effect spectroscopy (NOESY) and ^{1}H-^{13}C heteronuclear single quantum coherence (HSQC) spectra of the hTERT022[T3T11] G-quadruplex in complex with ZBH-01 or CPT-11. ^{1}H-^{13}C HSQC analysis revealed significant CSPs at 5'-flanking (A1, A2, T3) and 3'-flanking (G20, C21, and C22) nucleotides, confirming ligand engagement at both terminal regions (Fig. 3G). Notably, the 3'-G-tetrad interface exhibited stronger CSPs in ^{1}H-^{13}C HSQC spectra and more ^{1}H-^{1}H NOE cross peaks, indicating preferential ligand interaction with the 3'-end (Fig. 3G).

We determined the three-dimensional (3D) structures of the hTERT022[T3T11] in complex with CPT-11 or ZBH-01 (Fig. 3H-J, Supplementary Fig. 6D, E, and Supplementary Table 2)[40,48]. The final root-mean-square deviations (RMSDs) of 0.15 ± 0.045 Å and 0.21 ± 0.041 Å for the backbone atoms confirm that these structural models are well-defined (Supplementary Table 2). The resolved 3D structures reveal that hTERT022[T3T11] adopts a canonical three-layered parallel G4 core, resembling other parallel-stranded G4 scaffolds (Fig. 3H–J)[30]. All guanines (G4–G6, G8–G10, G14–G16 and G18–G20) adopt anti-glycosidic conformations, forming clockwise hydrogen-bond networks within each G-tetrad (Fig. 3H–J). The three double-chain-reversal loops connect the G-tetrad layers, stabilized by centrally coordinated K^{+} ions (Fig. 3H-J).

Structural alignment showed that CPT-11 and ZBH-01 adopt similar orientations within the G4 binding pocket, flanked by conserved guanines and 3'-terminal nucleotides (Fig. 3H–J). Specifically, both ligands stack heterocyclic rings onto the external G-tetrad (G6/G10) via π-π interactions, while their E-rings engage with 3'-flanking bases (C21/C22) (Fig. 3H–J). Hydrophobic contacts between ethyl groups (E-/B-rings) and G6/G10 purines provide additional stabilization (Fig. 3H–J). Notably, a key distinction emerged in their side-chain interactions. CPT-11's bis-piperidines moiety forms hydrophobic contacts with G14 and G15, while the *N*-methylpiperazine of ZBH-01 remains solvent-exposed, suggesting differential binding interactions (Fig. 3J).

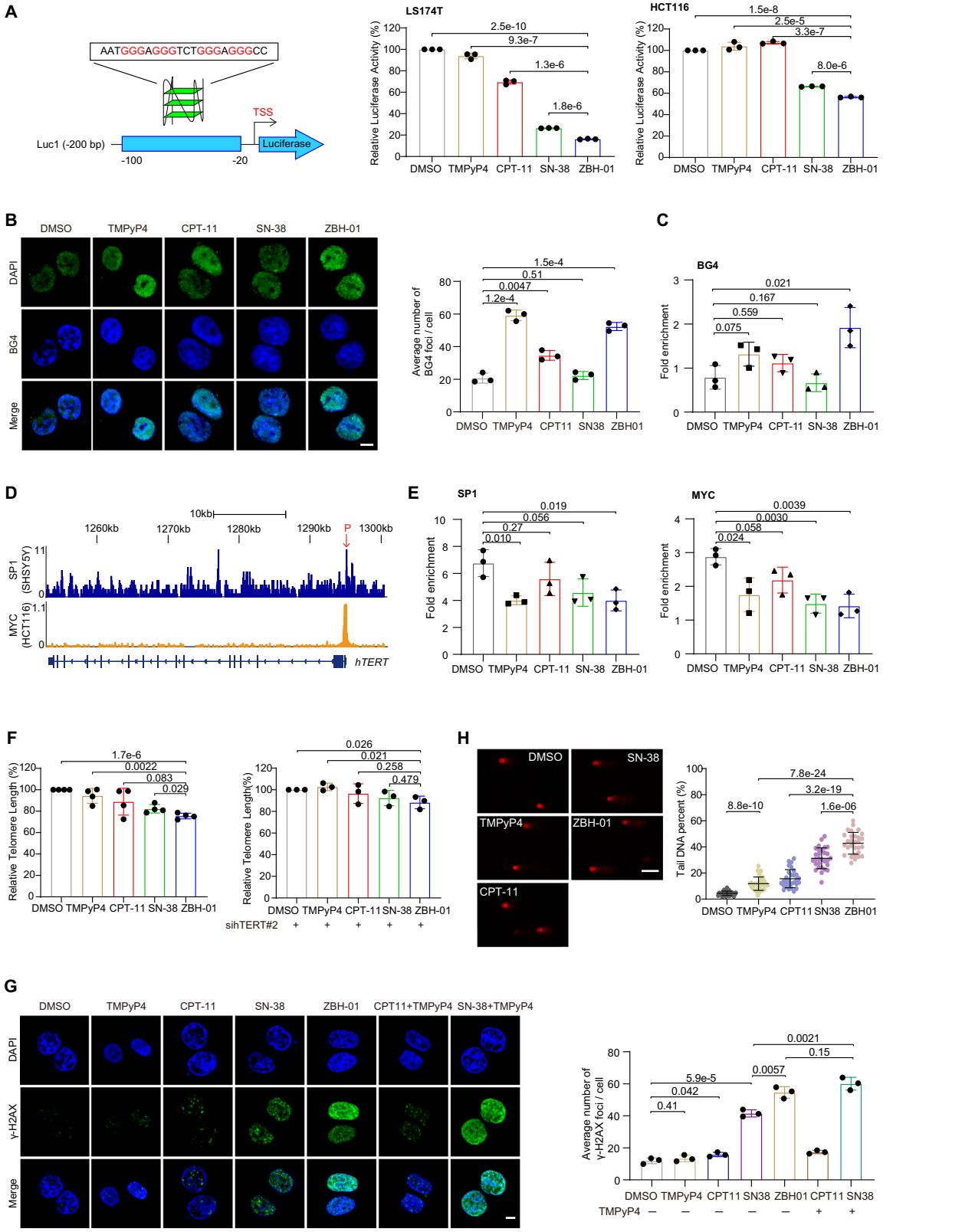

ZBH-01 induces DNA damage and telomere shortening through dual-targeting mechanisms

To systematically evaluate the dual-target capacity of ZBH-01, we developed a luciferase reporter assay containing the critical G4 forming region of the *hTERT* promoter (-350 to +12 bp relative to the transcription start site, TSS; Fig. 4A). ZBH-01 treatment potently suppressed *hTERT* promoter activity by 84% in LS174T cells and 44% in HCT116 cells (Fig. 4A and Supplementary Fig. 7A), consistent with its downregulation of endogenous *hTERT* mRNA (Fig. 2D). Comparative analysis revealed that ZBH-01 had stronger effects than TMPyP4 (6.1% inhibition in LS174T) and CPT-11 (31% in LS174T), while achieving suppression comparable to SN-38 (73% reduction in LS174T; 34% in HCT116) (Fig. 4A and Supplementary Fig. 7A). This similar efficacy resulted from fundamentally distinct modes of action: ZBH-01-mediated suppression resulted from direct dual targeting of

Fig. 4 | ZBH-01 targets the *hTERT* promoter to induce telomere shortening, DNA damage and genome instability. A Schematic representation of the hTERT-luciferase reporter construct (left). The PGL3 plasmid carrying the *hTERT* core promoter region with the G4-DNA sequence was transfected into LS174T and HCT116 cells. Luciferase activity was measured following treatment of DMSO, ZBH-01 (200 nM), SN-38 (200 nM), CPT-11 (1 μM) or TMPyP4 (1 μM) for 24 h. The luciferase activity in DMSO-treated cells was set as 100%. Quantitative data (right) are represented as mean ± S.D. ($n \geq 3$ independent experiments). *p*-values were determined using a two-tailed unpaired Student's *t*-test. **B** Detection of G4s foci by immunofluorescence (IF). LS174T cells were treated with DMSO, ZBH-01 (100 nM), SN-38 (100 nM), CPT-11 (500 nM), or TMPyP4 (500 nM) for 24 h and stained using the BG4 antibody (green) for G-quadruplex visualization. Nuclei were counterstained with DAPI (blue). Scalar bars: 5 μm. Quantitative data (right) are represented as mean ± SEM ($n \geq 3$ independent experiments). *p*-values were determined using a two-tailed unpaired Student's *t*-test. **C** ChIP-qPCR analysis of G-quadruplex enrichment at the *hTERT* promoter region in LS174T cells treated with DMSO, ZBH-01 (100 nM), SN-38 (100 nM), CPT-11 (500 nM) or TMPyP4 (500 nM) for 24 h. Data are shown as mean ± SEM ($n \geq 3$ independent experiments). *p*-values were calculated using a two-tailed unpaired Student's *t*-test. **D** ChIP-seq dataset analysis (GSE184957, GSE181450) showing SP1 and MYC enrichment at the *hTERT* promoter region. The red arrow highlights the G4-DNA site selected for ChIP-qPCR analysis. **E** ChIP-qPCR analysis of SP1 and MYC at the *hTERT* promoter region in LS174T cells treated with DMSO, ZBH-01 (100 nM), SN-38 (100 nM), CPT-11 (500 nM) or TMPyP4 (500 nM) for 24 h. Data are shown as mean ± SEM ($n \geq 3$ independent experiments). *p*-values were calculated using a two-tailed unpaired Student's *t*-test. **F** Relative telomere length analysis in LS174T cells treated for 5 days with DMSO, ZBH-01 (200 nM), SN-38 (200 nM), CPT-11 (1 μM), or TMPyP4 (1 μM) under control (left) or hTERT-knockdown conditions (right). For knockdown experiments, cells were transfected with *hTERT*-targeting siRNA (sihTERT) for 6 h prior to compound treatment. Genomic DNA was extracted and telomere length was quantified by qPCR, normalized to the single-copy gene 36B4 (ΔCt). Data represent mean ± SD from ≥3 independent experiments. *p*-values were determined using a two-tailed unpaired Student's *t*-test. **G** Detection of γ-H2AX foci by immunofluorescence (IF). LS174T cells were treated with DMSO, ZBH-01 (100 nM), SN-38 (100 nM), CPT-11 (500 nM), or TMPyP4 (500 nM) for 48 h and stained using the γ-H2AX antibody (green). Nuclei were counterstained with DAPI (blue). Scalar bars: 5 μm. Quantitative data (right) are represented as mean ± SEM ($n \geq 3$ independent experiments). *p*-values were determined using a two-tailed unpaired Student's *t*-test. **H** Comet assay measuring DNA fragmentation in LS174T cells after 48-h treatment with DMSO, TMPyP4 (500 nM), CPT-11 (500 nM), SN-38 (100 nM) or ZBH-01 (100 nM). Scalar bars: 50 μm. Tail DNA percentage was quantified using ImageJ. Data are presented as mean ± S.D. ($n \geq 3$ independent experiments). *p*-values were determined using a two-tailed unpaired Student's *t*-test.

both TOP1 and G4 structures, whereas SN-38's effects likely occurred indirectly through DNA damage response without G4 engagement.

Using G4-specific antibody (BG4) staining, our immunofluorescence results confirmed that TMPyP4 treatment significantly enhanced nuclear G4 formation in LS174T cells (Fig. 4B). Notably, ZBH-01 and CPT-11 also induced substantial G4 stabilization (~2-fold increase in BG4 signal), while SN-38 showed minimal effect (Fig. 4B). Chromatin immunoprecipitation assays (ChIP) specifically targeting the *hTERT* promoter G4 region demonstrated that ZBH-01 treatment generated the strongest BG4 enrichment (143% increase), significantly exceeding TMPyP4 (67%) and CPT-11 (41%) (Fig. 4C), validating its potent G4-stabilizing capability at the target promoter.

The *hTERT* promoter features a critical G4-E-box motif located 199 bp upstream of TSS (Fig. 4D). This motif serves as a binding platform for oncogenic transcription factors MYC and SP1[49–51], which cooperatively drive differential *hTERT* expression. Notably, ChIP assays showed that ZBH-01 treatment reduced SP1 and MYC binding at the *hTERT* promoter by 41% and 51%, respectively (Fig. 4E), exceeding effect of TMPyP4 (39–41% reduction) and CPT-11 (17–24% reduction) (Fig. 4E). Notably, this disruption occurred despite the moderate G4 binding affinity of ZBH-01 (K_d ~ 48.5 μM) compared to the G4 stabilizer TMPyP4 (K_d ~ 0.35 μM). This efficacy of ZBH-01 results from two complementary mechanisms. Direct G4 stabilization displaces transcription factors at the *hTERT* promoter, while concurrent suppression of MYC protein levels (25% reduction; Supplementary Fig. 7B) may further diminish SP1/MYC occupancy (41–51% removal). In contrast, SN-38-mediated *hTERT* suppression occurs indirectly through DNA damage-induced MYC downregulation without direct G4 engagement (Fig. 2D, E, Supplementary Fig. 7B).

To evaluate functional consequences, we analyzed telomere dynamics and DNA damage responses. Quantitative telomere length analysis demonstrated that ZBH-01 treatment (200 nM, 5 days) induced significant telomere shortening (24% reduction) in LS174T cells, exceeding the effects of SN-38 (18%), TMPyP4 (5.6%) and CPT-11 (11%) (Fig. 4F). To determine the dependency of this effect on hTERT suppression, we performed siRNA-mediated hTERT knockdown (Supplementary Fig. 7C). hTERT knockdown attenuated ZBH-01-induced telomere shortening to 12% (Fig. 4F), supporting a primary role for hTERT suppression, with residual activity likely reflecting complementary TOP1-mediated DNA damage.

We next assessed DNA damage responses by analyzing phosphorylated histone H2AX (γ-H2AX) levels in LS174T cells. Immunofluorescence analysis showed that ZBH-01 treatment generated more γ-H2AX foci per cell (4.6-fold increase over DMSO controls) than single-agent treatment with TMPyP4 (1.1-fold increase), CPT-11 (1.3-fold increase), or SN-38 (3.5-fold increase). Notably, the efficacy of ZBH-01 exceeded that of TMPyP4+CPT-11 co-treatment (3.1-fold increase) and matched the TMPyP4+SN-38 combination (Fig. 4G). Western blot analysis confirmed elevated γ-H2AX protein levels under ZBH-01 treatment (Supplementary Fig. 7D). ZBH-01treatment increased global γ-H2AX levels by 60%, exceeding the increases induced by TMPyP4 (4%), CPT-11 (12%), and SN-38 (49%), as well as the TMPyP4+CPT-11 co-treatment (12%) (Supplementary Fig. 7D). Notably, ZBH-01 showed comparable effects to the TMPyP4+SN-38 combination (Supplementary Fig. 7D). Alkaline comet assays further demonstrated enhanced genotoxic activity, showing that ZBH-01-treated LS174T cells exhibited significantly longer comet tails (9.6-fold increase over controls) compared to SN-38 (7.0-fold), TMPyP4 (2.7-fold), and CPT-11 (3.5-fold) (Fig. 4H). Consistent results in HCT116 cells confirmed broad pharmacological efficacy (Supplementary Fig. 7E). Together, these findings illustrate that ZBH-01 induces DNA damage through coordinated G4 stabilization and TOP1 inhibition, highlighting the potential advantage of its dual-mechanism approach over single-target strategies.

ZBH-01 induces senescence in CRC cells

To evaluate the capacity of ZBH-01 to drive cellular senescence, we performed senescence-associated β-galactosidase (SA-β-gal) activity assays in CRC cells. In LS174T cells, ZBH-01 or SN-38 treatment (100 nM, 48 h) significantly increased SA-β-gal-positive cells, whereas CPT-11, TMPyP4, or their combination showed minimal effects (Fig. 5A and Supplementary Fig. 8A). ZBH-01 demonstrated enhanced efficacy, producing a 30% greater increase in senescent cells than SN-38 alone and matching the effect of SN-38 combined with TMPyP4 (Fig. 5A and Supplementary Fig. 8A). Notably, senescence induction was significantly attenuated in hTERT-knockdown LS174T cells. While ZBH-01 treatment increased SA-β-gal-positive cells by 60% in control cells, this effect was reduced to 15% in hTERT-knockdown cells, confirming the hTERT dependency (Fig. 5A and Supplementary Fig. 8B). Consistent senescence results in SW480 cells validated this hTERT-dependent mechanism (Supplementary Fig. 8C, D), establishing hTERT as the primary therapeutic target while highlighting the contribution of complementary TOP1 inhibition-mediated genomic instability to the senescence response.

We next examined heterochromatin formation using histone H3 lysine 9 tri-methylation (H3K9me3), a marker for senescence-associated heterochromatin foci (SAHF). Immunofluorescence analysis revealed that ZBH-01 or SN-38 treatment significantly increased H3K9me3-positive foci,

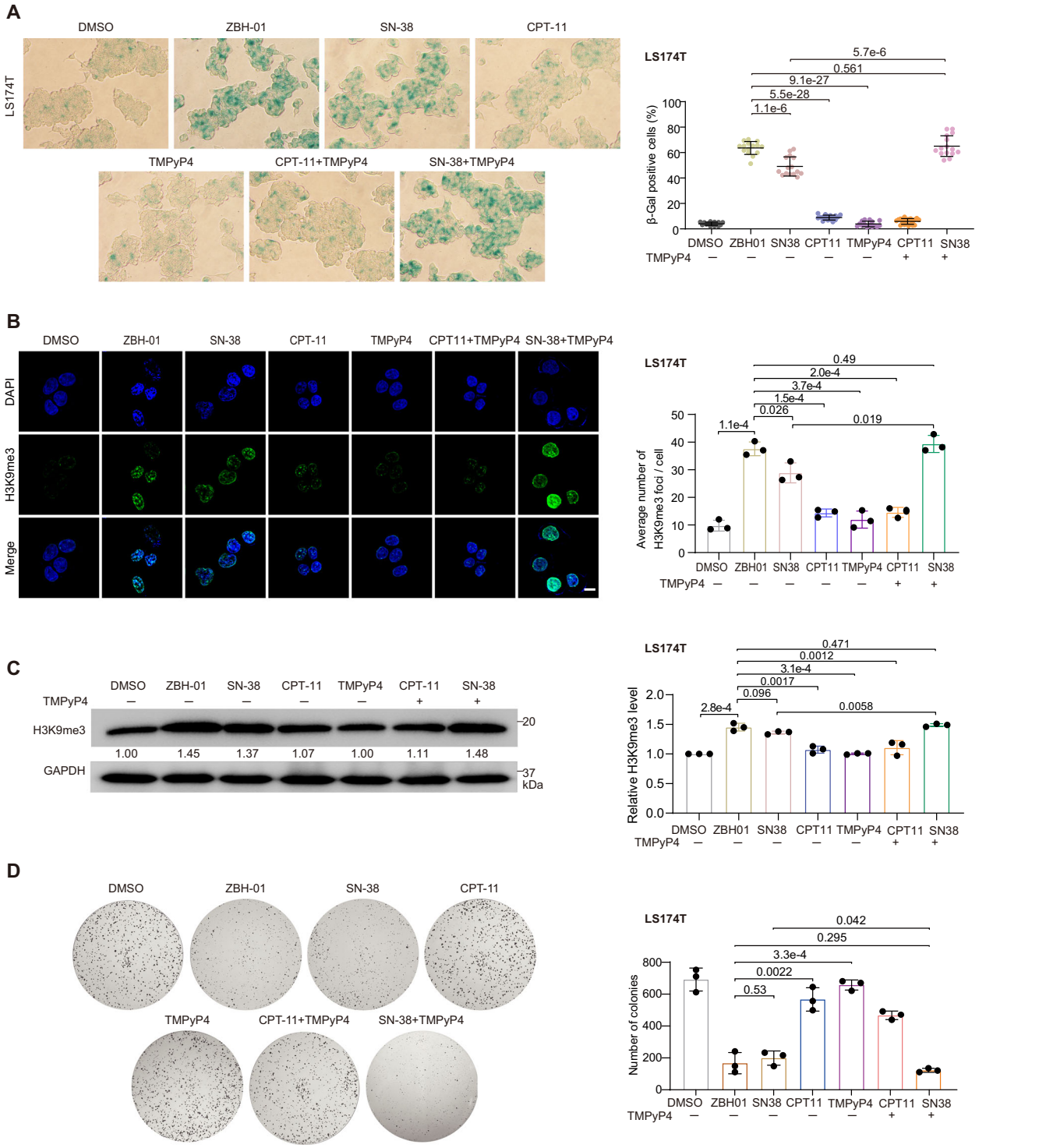

Fig. 5 | ZBH-01 suppresses cell growth and induces senescence. A Senescence-associated β-galactosidase (SA-β-gal) staining in LS174T cells treated with DMSO, ZBH-01 (100 nM), SN-38 (100 nM), CPT-11 (500 nM), TMPyP4 (500 nM) or the combinations of CPT-11 + TMPyP4, and SN-38 + TMPyP4 for 48 h. Magnification: 40x. Quantitative analysis (right) shows the percentage of SA-β-Gal-positive cells, presented as mean ± S.D. ($n \geq 3$ independent experiments). *p*-values were determined using a two-tailed unpaired Student's *t*-test. **B** Immunofluorescence detection of H3K9me3 foci in LS174T cells treated with DMSO, ZBH-01 (100 nM), SN-38 (100 nM), CPT-11 (500 nM), or TMPyP4 (500 nM) for 48 h and stained with H3K9me3 antibody (green). Nuclei were counterstained with DAPI (blue). Scalar bars: 10 μm. Quantitative data (right) are represented as mean ± SEM ($n \geq 3$ independent experiments). *p*-values were determined using a two-tailed unpaired Student's *t*-test. **C** Western blot analysis of H3K9me3 protein levels in LS174T cells treated with DMSO, ZBH-01 (100 nM), SN-38 (100 nM), CPT-11 (500 nM), TMPyP4 (500 nM) or the combinations of CPT-11 + TMPyP4, and SN-38 + TMPyP4 for 48 h. Quantitative data are represented as mean ± S.D. ($n \geq 3$ independent experiments). Relative expression was normalized to GAPDH. *p*-values were determined using a two-tailed unpaired Student's *t*-test. **D** Colony formation assay in LS174T cells over 12 days. LS174T cells were treated with DMSO, ZBH-01 (1 nM), SN-38 (1 nM), CPT-11 (5 nM), TMPyP4 (5 nM) or drug combinations. Quantitative data represent mean ± S.D. ($n \geq 3$ independent experiments). *p*-values were determined using a two-tailed unpaired Student's *t*-test.

whereas CPT-11, TMPyP4, or their combination showed minimal effects (Fig. 5B). ZBH-01 demonstrated a 30% greater increase in H3K9me3-staining than SN-38 alone (Fig. 5B), indicating enhanced locus-specific heterochromatin formation. Western blot analysis confirmed that ZBH-01 treatment increased global H3K9me3 levels, exceeding those induced by SN-38, CPT-11, TMPyP4, or their combinations (Fig. 5C). While the induction effect of ZBH-01 was slightly weaker than the SN-38 + TMPyP4 combination (Fig. 5B, C), these results underscore the importance of coordinated TOP1 inhibition and G4 targeting for optimal heterochromatin induction.

Colony formation assays validated the anti-proliferative activity of ZBH-01, showing greater suppression in LS174T, HCT116, and SW480 cells than CPT-11, TMPyP4, or their combination (Fig. 5D and Supplementary Fig. 9A, B). ZBH-01 exhibited improved performance compared to SN-38 monotherapy and achieved comparable efficacy to the combination of SN-38 with TMPyP4 (Fig. 5D and Supplementary Fig. 9A, B). Quantitative analysis revealed that the TMPyP4+SN-38 combination reduced colony formation by 40% more than SN-38 alone ($p = 0.042$), while ZBH-01 as a single agent showed statistically equivalent efficacy to this combination ($p = 0.295$; Fig. 5D). Notably, the performance of ZBH-01 treatment significantly exceeded both CPT-11 monotherapy (71% greater suppression) and TMPyP4 alone (75% greater suppression), while also surpassing the TMPyP4+CPT-11 combination (64% greater suppression; Fig. 5D). These results demonstrate that dual targeting of TOP1 and G4 can produce efficacy comparable to combination therapies while maintaining the pharmacological advantages of a single molecular entity.

ZBH-01 suppresses chemoresistance and enhances drug sensitivity in CRC models

Given the clinical challenge of chemoresistance to cornerstone CRC therapies cisplatin (DDP) and 5-fluorouracil (5-FU) [9,52], we evaluated the efficacy of ZBH-01 in resistant models through MTT assays. In DDP-resistant HCT116-DDP cells ($IC_{50} = 117.3$ μM), ZBH-01 demonstrated remarkable potency ($IC_{50} = 2.3$ μM), exhibiting 14-fold and 7-fold greater efficacy than CPT-11 ($IC_{50} = 33.2$ μM) and SN-38 ($IC_{50} = 16.5$ μM), respectively (Fig. 6A, B and Supplementary Fig. 10). Similarly, in 5-FU-resistant HCT8-5-FU cells ($IC_{50} = 2.9$ μM), ZBH-01 ($IC_{50} = 0.071$ μM) outperformed CPT-11 by 61-fold and SN-38 by 2.4-fold (Fig. 6A, B and Supplementary Fig. 10). We next investigated ZBH-01's potential in combination regimens. Using a fixed ZBH-01 concentration (10 nM or 1 μM) with serially diluted chemotherapeutics, we observed synergistic enhancement: the 5-FU IC_{50} decreased 2.5-fold (from 2.9 to 1.15 μM) while the DDP IC_{50} decreased 8.9-fold (from 117.3 to 13.2 μM) in their respective resistant models (Fig. 6A, B and Supplementary Fig. 10).

To characterize drug interactions, we conducted quantitative combination index (CI) analysis using the Chou-Talalay method in resistant HCT116-DDP cells. ZBH-01 combined with DDP demonstrated synergistic interactions ($CI < 0.9$) at sub-IC_{50} concentrations, with particularly strong synergy (CI = 0.12–0.16) achieved with 2–16 μM ZBH-01 combined with 12.5 μM DDP (maximal synergy CI = 0.12 at 4 μM ZBH-01 + 12.5 μM DDP) (Fig. 6C). Notably, antagonistic effects ($CI > 1.1$) emerged at DDP concentrations exceeding 200 μM, accompanied by decreased relative inhibition (RI) values (Fig. 6C), highlighting the importance of careful dose optimization for therapeutic efficacy. This concentration-dependent synergy likely comes from complementary mechanisms: ZBH-01 induces DNA damage and epigenetic modulation via dual TOP1/G4 targeting, while DDP creates distinct DNA lesions. These findings highlight the importance of precise dosing for clinical translation.

RT-qPCR analysis showed that ZBH-01 treatment profoundly reduced mRNA levels of cell cycle regulators (*CCNA2*, *CDC25A*), senescence drivers (*MYBL2*), and immortality-associated genes (*hTERT*, *MYC*) in HCT116-DDP cells, exceeding effects of SN-38, DDP, and CPT-11 (Fig. 6D). Additionally, ZBH-01 demonstrated enhanced efficacy against multidrug resistance transporters (*ABCG2*, *ABCC1*) and DNA repair genes (*FANCD2*, *FANCI*, *FANCA*) (Fig. 6D), indicating its capacity to disrupt multidrug resistance while disrupting essential DNA maintenance pathways. Notably, the combination of ZBH-01 and DDP significantly enhanced pharmacological efficacy compared to single-agent treatments (Fig. 6D). These synergistic effects result from complementary mechanisms: ZBH-01's dual-targeting capacity (TOP1 inhibition and G4 stabilization) induces DNA damage and epigenetic modulation, while DDP creates DNA crosslinks and disrupts DNA repair. These results establish ZBH-01 and DDP combination as a promising therapeutic strategy against CRC.

Discussion

In this study, we introduce ZBH-01, a camptothecin derivative designed to integrate TOP1 inhibition with DNA G-quadruplex (G4) stabilization. Our comprehensive data demonstrate that ZBH-01 can address fundamental limitations of conventional single-mechanism therapies through its coordinated dual-targeting capabilities. Unlike CPT-11, which requires metabolic conversion to SN-38, ZBH-01 directly engages both TOP1 and G4 targets, simultaneously stabilizing the TOP1-DNA complex and binding oncogenic G4 structures in promoters such as *hTERT*. This dual activity induces proteasomal degradation through ubiquitin/SUMOylation pathways, while disrupting transcription factor binding (e.g., SP1, MYC), suppressing hTERT expression, and destabilizing telomere maintenance.

ZBH-01 exhibits promising therapeutic advantages, including over 2600-fold higher aqueous solubility than SN-38 while maintaining stability in vitro, enabling excipient-free formulation. Importantly, ZBH-01 demonstrated activity in chemoresistant models, exhibiting 14-fold and 7-fold greater efficacy than CPT-11 and SN-38, respectively, in cisplatin-resistant cells, and outperforming CPT-11 by 61-fold and SN-38 by 2.4-fold in 5-FU-resistant models. In combination regimens, ZBH-01 synergistically enhanced conventional chemotherapeutics, reducing IC_{50} values of 5-FU and cisplatin by 2.5-fold and 8.9-fold, respectively, in resistant models. This coordinated pharmacokinetic profile mitigates challenges of combination therapies where separate drugs may have mismatched absorption and distribution profiles.

Our findings align with recent discoveries demonstrating camptothecin derivatives with G4-binding activity[53], but ZBH-01 represents an advancement through its balanced design that overcomes pharmacokinetic limitations of existing therapies. While CPT-11 suffers low conversion efficiency and SN-38 undergoes rapid glucuronidation, ZBH-01 bypasses metabolic activation requirements and exhibits enhanced aqueous stability. This optimized profile enables ZBH-01 to achieve potency comparable to SN-38 in TOP1 inhibition while simultaneously engaging G4 structures, effectively matching the combined effects of SN-38 and TMPyP4 in a single molecule.

The therapeutic landscape of G4-targeting agents continues to progress with clinical-stage ligands including Pidnarulex (CX-5461) and Quarfloxin (CX-3543)[54,55]. CX-5461 is a G-quadruplex stabilizer in Phase I/II trials. It shows particular efficacy in patients with BRCA1/2 or PALB2 mutations[54], while CX-3543 targets nucleolin-associated G4s in the ribosomal DNA (rDNA)[55]. Unlike these mono G4-targeting agents, ZBH-01 combines moderate G4-binding affinity with potent TOP1 inhibition. This dual-mechanism approach enables simultaneous DNA damage induction and transcriptional repression through complementary pathways.

Structural analyses reveal how the rational design of ZBH-01 enables dual interactions through its N-methylpiperazine and N-formylglycine moieties facilitate G4 stabilization through groove binding and end-stacking interactions, while the preserved camptothecin core maintains effective TOP1 inhibition. Although steric constraints suggest opportunities for further optimization, this bifunctional design provides a valuable template for next-generation agents. Refining the N-formylglycine linker or α-hydroxyl lactone ring could enhance G4 accommodation and reduce hydrolytic susceptibility, potentially amplifying therapeutic efficacy.

The reported half-life of the hTERT mRNA is approximately 2–3 h[56], while hTERT protein half-life or the telomerase activity is about 5–11 h[57,58], depending on tumor cell type. This transient nature of hTERT regulation

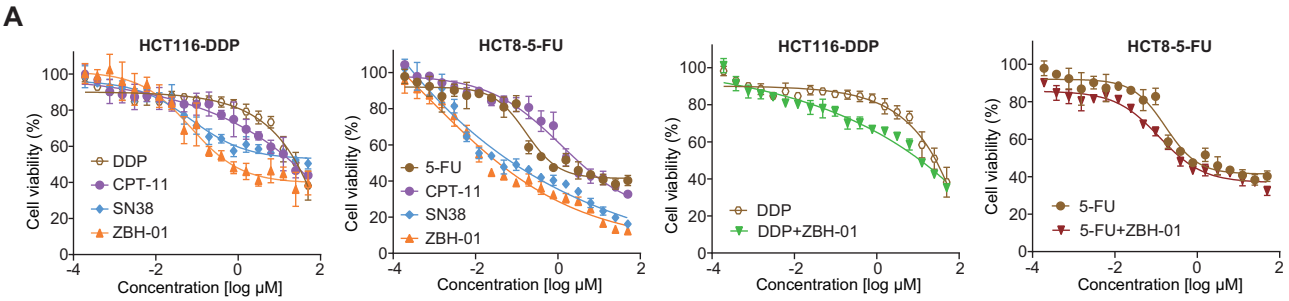

B

Compound	IC_{50} (μM)			
	HCT116	HCT116-DDP	HCT8	HCT8-5-FU
CPT11	4.00	33.16	2.16	4.35
SN38	0.029	16.54	0.045	0.17
ZBH01	0.026	2.33	0.021	0.071
DDP	1.80	117.26	-	-
DDP+ZBH01	-	13.22	-	-
5-FU	-	-	1.99	2.90
5-FU+ZBH-01	-	-	-	1.15

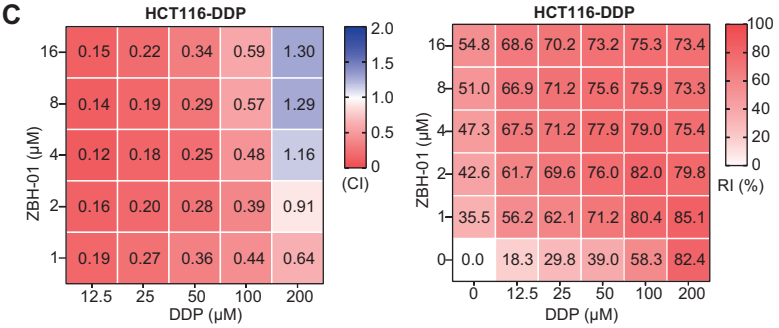

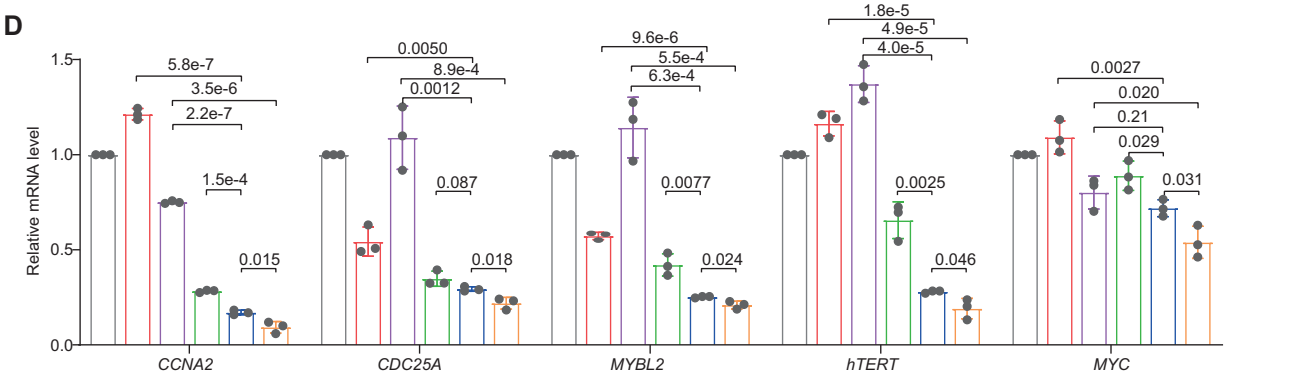

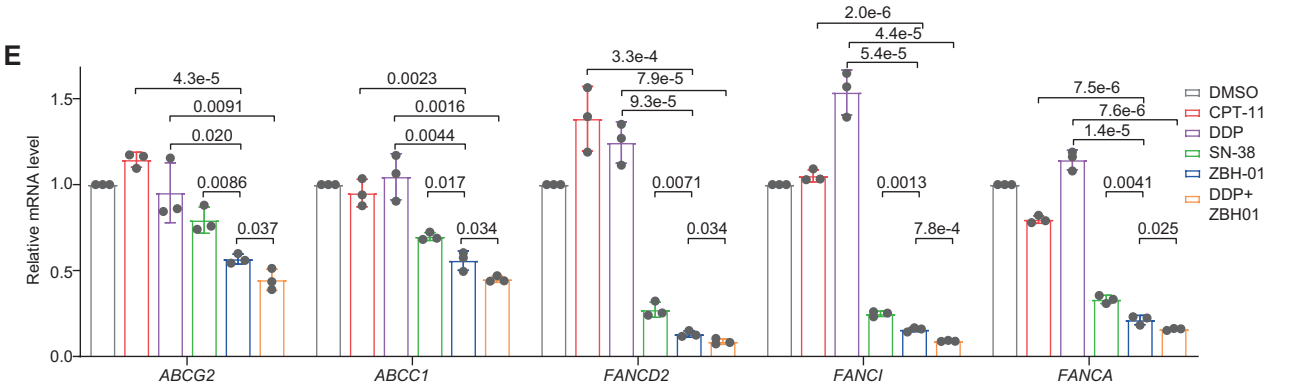

Fig. 6 | ZBH-01 enhances chemosensitivity in drug-resistant CRC models. **A**, **B** Inhibition of cell viability in HCT116-DDP and HCT8-5FU resistant cells treated with ZBH-01, CPT-11, SN-38, 5-FU, and DDP, or combination of ZBH-01 (10 nM) with 5-FU and ZBH-01 (1 μM) with DDP (MTT assay). Data represent mean ± SEM from at least three independent experiments. IC_{50} values were determined using IBM SPSS Statistics (Version 26). **C** Combination index (CI) and Relative inhibition (RI) analysis in HCT116-DDP cells treated with ZBH-01 and DDP at the indicated concentrations for 72 h. CI < 1 indicates synergy; CI < 0.3 indicates strong synergy; CI > 1 indicates antagonism. **D**, **E** RT-qPCR analysis of gene expression in HCT116-DDP cells after treatment for 24 h with DMSO, ZBH-01 (2 μM), SN-38 (2 μM), CPT-11 (2 μM), DDP (25 μM) or the combinations of ZBH-01 + DDP. Data are presented as mean ± S.D. ($n \geq 3$ independent experiments per condition). *p*-values for each comparison were determined using a two-tailed unpaired Student's *t*-test.

suggests that the sustained impacts we observed, including DNA damage, epigenetic silencing, and senescence, result from ZBH-01's dual mechanism initiating irreversible downstream biological processes rather than continuous telomerase inhibition. These lasting effects persist beyond initial treatment, highlighting the compound's capacity to trigger irreversible cellular responses.

Collectively, ZBH-01 represents a step forward in therapeutic strategies for CRC and potentially other malignancies. By simultaneously targeting

TOP1 and G4-mediated pathways, it impairs DNA repair mechanisms and transcriptional networks, re-sensitizing resistant cells while bypassing pharmacokinetic barriers that limit conventional therapies. This approach could effectively address cancer cell adaptability to single-pathway inhibition, a key driver of chemoresistance. Future work will explore structural refinements to optimize dual-binding kinetics and in vivo efficacy, particularly through modified linkers resistant to hydrolytic cleavage. By bridging DNA damage response and epigenetic regulation, ZBH-01 exemplifies the potential of multi-mechanistic targeting, offering a paradigm shift toward combinatorial, single-agent strategies.

Methods

ZBH-01 synthesis

The synthesis of ZBH-01 was performed as described in Supplementary Fig. 1[34]. In brief, benzyl-protected glycine hydrochloride was reacted with triphosgene in a biphasic system consisting of saturated sodium bicarbonate solution and dichloromethane to produce isocyanates. The isocyanates were then coupled with SN-38 in tetrahydrofuran (THF) in the presence of triethylamine (Et_3N). Catalytic hydrogenation (Pd/C) was subsequently used to remove the benzyl protecting groups, releasing free carboxylic acid groups. The carboxylic acids were acylated with *N*-methylpiperazine using the coupling reagents HBTU (*O*-benzotriazole-1-yl-*N*,*N*,*N*',*N*'-tetramethyluronium hexafluorophosphate) and DIEA (*N*,*N*-diisopropylethylamine). Finally, the product was converted to its hydrochloride salt by treatment with hydrochloric acid in ethyl acetate, yielding the target ZBH-01 compound.

Solubility determination

The solubility of ZBH-01 was determined using the shake-flask method. Briefly, an excess amount of ZBH-01 was added to water or phosphate buffers and the mixture was equilibrated for 24 h at 25 °C with constant shaking. The resulting saturated solution was then centrifuged at 16,200 × *g* for 20 min at 25 °C. The supernatant was carefully collected and filtered through a 0.22 μm membrane. The concentration of ZBH-01 in the supernatant was quantified by high-performance liquid chromatography (HPLC) using a standard calibration curve. HPLC analysis was performed on an Agilent 1260 Infinity system equipped with a Kromasil 100-5-C18 column (4.6 × 150 mm, 5 μm) maintained at 40 °C. The isocratic mobile phase consisted of acetonitrile and water containing 0.1% acetic acid (70:30, v/v), delivered at a flow rate of 1.0 mL/min. The effluent was monitored by a UV detector set at 280 nm. All measurements were performed in triplicate.

Stability determination

Samples of ZBH-01 were dissolved in 1.0 mL of either purified water or PBS (pH 7.4) and incubated at 25 °C for 24 h with shaking. After centrifugation at 16,200 × *g* for 20 min, the supernatant was filtered through a 0.22 μm membrane prior to analysis. Samples were analyzed using an Agilent 1260 HPLC system coupled to an Agilent 6460 triple quadrupole mass spectrometer (LC-MS). Chromatographic separation was achieved using a Kromasil 100-5-C18 column (4.6 × 150 mm, 5 μm) maintained at 40 °C. Compound stability was assessed by comparing chromatographic peak areas and mass spectra before and after the 24-h incubation period.

Cell culture

LS174T, HCT116, HCT8, SW480, A549, HeLa, MCF7 and PC3 cell lines were purchased from ATCC. LS174T, SW480, A549, HeLa, MCF7 cells were cultured in DMEM (Biological Industries) supplemented with 10% FBS (Biological Industries) and 1% Pen Strep (Gibco). HCT116, HCT8, PC3 cells were cultured in RPMI-1640 (Sigma-Aldrich) supplemented with 10% FBS (Biological Industries) and 1% Pen Strep (Gibco). All cell lines were cultured in a 5% CO_2 atmosphere at 37 °C. Cisplatin-resistance HCT116 cell line (HCT116-DDP) and 5-fluorouracil resistance HCT8 cell line (HCT8-5-FU) were purchased from Fenghui Biotechnology (Hunan, China). The HCT116-DDP cell line was cultured in RPMI-1640 (Sigma-Aldrich) supplemented with 10% FBS (Biological Industries), 1% Pen Strep (Gibco), and 1 μg/ml cisplatin (MCE, HY-17394) to maintain resistance. The HCT8-5-FU cell line was cultured in RPMI-1640 (Sigma-Aldrich) supplemented with 10% FBS (Biological Industries), 1% Pen Strep (Gibco), and 5 μg/ml 5-fluorouracil (MCE, HY-90006) to maintain resistance. All cell lines routinely tested for human pathogens and mycoplasma.

Cell viability assay

Cell viability was assessed using MTT assays. Different cell lines were plated in clear 96-well plates at 2500-5000 cells/well and allowed to attach overnight at 37 °C. The cells were then incubated with different concentrations of CPT-11 (Selleck, S2217), SN-38 (Selleck, S4908), ZBH-01 (synthesized by the Institute of Pharmacology and Toxicology, Chinese Academy of Military Medical Sciences, China) for 72 h. A total of 20 μL of MTT reagent was added to each well (final concentration: 0.5 mg/mL). After incubation for an additional 4 h at 37 °C, the supernatant was carefully removed, and 150 μL DMSO was added to each well. Absorbance was measured at 570 nm using a MULTISKAN GO (Thermo Fisher). All experiments were repeated three times.

Synergism analysis

HCT116-DDP cells were treated for 72 h with ZBH-01, DDP, or both at varying concentrations, followed by an MTT assay. The synergism of the drug combinations was evaluated using CompuSyn (ComboSyn, Inc.), which is based on the median-effect principle established by Chou and Talalay[59]. The combination index (CI) for each dose combination was calculated. Synergism, additive effect, and antagonism were defined by CI values of <1.0, =1.0, and >1.0, respectively.

Immunocomplex of enzyme (ICE) bioassay

TOP1-DNA covalent complexes were isolated using the Immunocomplex of Enzyme (ICE) bioassay. LS174T cells were cultured in 100 mm Petri dishes until they reached 90% confluence (approximately 1×10^7 cells). The culture medium was supplemented with 4 μM of CPT-11, SN-38 or ZBH-01, respectively, while the control group received an equivalent volume of DMSO. After incubation at 37 °C for 30 min, the medium was removed, and the cells were lysed with 2 mL of 1% sarkosyl (Shanghai Sig Biotech). A discontinuous four-layer CsCl density gradient was prepared by layering 2 mL of CsCl solution per layer, with decreasing density from bottom to top. The cell lysates were gently layered on the CsCl gradient and centrifuged at 125,000 × *g* for 20 h at 20 °C. Following centrifugation, 400 μL fractions were collected from the bottom of the tube. Each fraction was diluted with an equal volume of 25 mM sodium phosphate buffer (pH 6.5) and applied to a nitrocellulose membrane using a slot-blot vacuum manifold. TOP1 protein and TOP1-DNA complexes were detected by Western blot analysis with anti-TOP1 monoclonal antibody (Abcam, ab32020).

Immunoblot analysis

Cells were lysed in RIPA buffer (Solarbio) containing PMSF (Solarbio), a Proteinase Inhibitor Cocktail (TransGen Biotech), and PhosSTOP (Roche). The concentration of total cellular protein was determined with the Enhanced BCA Protein Assay Kit (Beyotime Biotechnology). The cell extracts were mixed with 5× Protein SDS-PAGE loading buffer (Takara) and heated at 104 °C for 10 min. Equal amounts of protein were loaded and analyzed by immunoblotting following standard protocols. Proteins were detected using specific antibodies at optimized dilutions (e.g., 1:1000 for primary antibodies; see Supplementary Table 3 for details) and visualized with SuperSignal West Femto Maximum Sensitivity Substrate (Thermo Fisher). Signal intensity was quantified using ImageJ software (v1.52a).

Molecular docking

The X-ray crystal structure of the human TOP1-DNA complex bound to camptothecin (PDB code: 1T8I) was retrieved from the Protein Data Bank (PDB). The 2D structures of ZBH-01, SN-38 and CPT-11 were generated using ChemDraw (RRID:SCR_016768). Protein structures were prepared using the "Protein Preparation Wizard" module in Maestro 11.8

(Schrödinger, New York, NY, United States, RRID: SCR_016748) with default parameters. The 3D structures of the small molecules were prepared using the "LigPrep" module, and molecular docking studies were performed using the "Glide" program in Maestro. The docking models were visualized and analyzed using PyMOL (DeLano Scientific, Palo Alto, CA, USA, RRID:SCR_000305).

RNA-seq analysis

LS174T cells were treated with DMSO, ZBH-01 (100 nM), SN-38 (100 nM), or CPT-11 (500 nM) for 24 h. Cells were pelleted by centrifugation, snap-frozen in liquid nitrogen, and stored at −80 °C. RNA sequencing libraries were constructed and sequenced by BGI Company (Wuhan, China; project number: F23A040005707_HOMgifoN). Clean reads were aligned to reference gene sequences using Bowtie2 (RRID:SCR_016368), and gene expression levels were quantified using RSEM (v1.2.8, RRID:SCR_000262). Differential gene expression analysis was performed with DEseq2 (RRID: SCR_015687), and heatmaps were generated using the R package pheatmap (RRID: SCR_016418). Data were analyzed via the UW Genetics Dr. Tom's Multi-Omics Integrated Analysis website (https://biosys.bgi. com/#/report/login).

Real-Time quantitative Polymerase Chain Reaction (RT-qPCR)

LS174T cells were treated as described for RNA-seq. Total RNA was extracted using RNAiso Plus reagent (Takara). cDNA was synthesized with Hifair III 1st Strand cDNA Synthesis SuperMix (Yeasen), and qPCR was performed on a LightCycler system (Roche) using SYBR Green Master Mix (Yeasen). Data were normalized to *GAPDH* expression, and relative expression changes were calculated using the $2^{-\Delta\Delta Ct}$ method. Gene-specific primers (Supplementary Table 4) were synthesized by Comate Bioscience Co., Ltd (Jilin, China). All experiments were repeated four times.

Oligonucleotides

DNA oligonucleotides (sequences in Table 1 and Supplementary Table 1) were synthesized by Sangon Biotech (Shanghai, China).

Nuclear Magnetic Resonance (NMR) spectroscopy

DNA samples for NMR were prepared in 20 mM potassium phosphate (KPi) and 70 mM KCl buffer (pH 7.0) in D_2O/H_2O (10%/90%). Lyophilized D_2O samples were redissolved in 99.98% D_2O. Samples were heated to 95 °C for 5 min and slowly cooled to room temperature (final DNA concentration: 0.15–2 mM). NMR experiments were performed on Bruker 600 and 800 MHz spectrometers (15–25°C). Spectral assignments were confirmed by NOESY (mixing time: 250–350 ms) and ^{1}H-^{13}C-HSQC. Data were processed with NMRPipe (v2.0)[60] and analyzed with NMRView (v5.0)[61].

Structure calculation

The high-resolution structures of the hTERT G4 in complexe with CPT-11 or ZBH-01 were calculated using the CNS[62] program through the distance geometry-simulated annealing protocol. Automatic iterative NOE assignment for the calculated structures was then performed using ARIA for optimization[63]. Hydrogen bonding constraints, interproton distance constraints, dihedral angle constraints, G-tetrahedral planarity constraints, and steric repulsion constraints were applied during calculations. The obtained structures were evaluated using CNS (v1.5) and ARIA (v2.0)[62,63]. 20 lowest-energy structures out of 200 structures were finally selected. Detailed constraints and validation statistics for the final structures are provided in Supplementary Table 2. The structures were displayed using the PyMOL program.

Circular dichroism (CD) spectroscopy

CD spectra were recorded on a MOS-450 spectropolarimeter (Biologic, China) using a 1 cm path length cuvette. DNA samples (5 μM) in 20 mM KPi and 70 mM KCl buffer (pH 7.0) were heated to 95 °C for 5 min and slowly cooled to room temperature. Compound concentration was 15 μM. Spectra were scanned from 230 and 330 nm at 25 °C.

Isothermal titration calorimetry (ITC)

ITC experiments were performed using a MicroCal iTC200 system (Malvern). DNA samples were prepared at a final concentration of 200 μM in a buffer containing 20 mM KPi and 70 mM KCl (pH 7.0), heated to 95 °C for 5 min, and slowly cooled to room temperature. A total of 250 μL of DNA solution was loaded into the sample cell, followed by titration with 2 mM compounds dissolved in the same buffer at 25 °C. A total of 20 injections were performed: 1 initial injection of 0.4 μL and 19 subsequent injections of 2 μL each. Data were analyzed using Origin software (MicroCal, RRID:SCR_002815), and dissociation constants (K_d) were calculated as the reciprocal of the association constant (K_a).

Luciferase assay

The pGL3 luciferase construct (RRID: Addgene_48743) containing the *hTERT* core promoter sequence (spanning −350 bp to +12 relative to the transcription start site) was constructed by Sangon-Biotech (China). LS174T or HCT116 cells were seeded in 12-well plates and cultured in serum-free medium. The cells were transfected with 400 ng pGL3 and 10 ng pRL-TK using PEI. After 6 h of culture, the medium was replaced with fresh medium containing 10% FBS, and the cells were treated with DMSO, ZBH-01 (200 nM), SN-38 (200 nM), CPT-11 (1 μM) or TMPyP4 (1 μM, Selleck, P1202). Following incubation for 6, 12, or 24 h, the cells were lysed with passive lysis buffer, and dual luciferase activity was measured with a Glo-Max® 20/20 fluorometer (Promega). The relative ratio of firefly to Renilla luciferase activity was calculated and normalized to the DMSO control. All experiments were repeated three times.

Immunofluorescence (IF)

LS174T cells were treated with DMSO, ZBH-01 (100 nM), SN-38 (100 nM), CPT-11 (500 nM), TMPyP4 (500 nM) or the indicated combination of CPT-11 (500 nM) and TMPyP4 (500 nM), SN-38 (100 nM) and TMPyP4 (500 nM) for 24 or 48 h. After treatment, cells were fixed with 4% paraformaldehyde for 10 min at room temperature, permeabilized with 0.1% Triton X-100 in PBS for 30 min, and blocked with a solution containing 3% BSA and 2% goat serum in PBS for 60 min. Cells were then incubated overnight at 4 °C with the following primary antibodies: anti-DNA G-quadruplex antibody BG4 (Merck Millipore, MABE917, 1:500); anti-trimethyl-Histone H3-Lys9 antibody (H3K9Me3, PTM BIO, PTM-616, 1:500); anti-g-H2AX antibody (Abcam, ab2893, 1:5000). After incubation, cells were washed three times with permeabilization buffer. Secondary antibodies used were: Goat anti-Rabbit IgG (H + L) Cross-Adsorbed Secondary Antibody, Alexa Fluor™ 488 (Invitrogen, A11034, 1:1000). Nuclei were counterstained with 4,6-diamidino-2-phenylindole (DAPI). Images were captured on an Olympus Confocal microscope (FV3000) using cellSens Standard (v1.18) software.

Foci quantification

Image analysis was performed using Fiji (ImageJ, v1.52). Following background subtraction, individual nuclei were segmented as Regions of Interest (ROIs) by thresholding the DAPI channel and applying the Watershed algorithm. Punctate foci within each fluorescence channel were identified using the Find Maxima function, with the Noise tolerance parameter calibrated for each experiment against raw images to distinguish specific foci from diffuse background. Cells showing only diffuse fluorescence were excluded. Nuclear ROIs were overlaid to restrict counts to intranuclear signals. Foci per nucleus were measured using the ROI Manager and exported to GraphPad Prism 9 for analysis. This standardized approach ensured consistent quantification across all conditions.

Chromatin immunoprecipitation (ChIP)

LS174T cells were treated with DMSO, ZBH-01 (100 nM), SN-38 (100 nM), CPT-11 (500 nM) or TMPyP4 (500 nM) for 24 h. Cells were cross-linked with 1% formaldehyde for 10 min at room temperature and then treated with 0.125 M glycine for 5 min to terminate cross-linking. Cells were washed with prechilled PBS and centrifuged at 1690 × *g* for 5 min at 4 °C.

The cells were resuspended in SDS lysis buffer and incubated at 4 °C for 10 min; chromatin was then sonicated into fragments of 300–400 bp using a Bioruptor sonicator (Diagenode). Chromatin was immunoprecipitated using 2 μg of the following antibodies: anti-DNA G-quadruplex antibody BG4 (Merck Millipore, MABE917), anti-MYC (Abcam, ab32072), anti-SP1 (Abcam, ab231778), with normal rabbit IgG as a control. DNA was eluted in elution buffer and analyzed by qPCR using SYBR Green Master Mix (Yeasen) on a LightCycler system (Roche). Primer sequences are listed in Supplementary Table 2.

Telomere length determination

LS174T cells were treated with DMSO, ZBH-01 (200 nM), SN-38 (200 nM), CPT-11 (1 μM), and TMPyP4 (1 μM) for 5 days, and genomic DNA (gDNA) was extracted using a DNA extraction kit (Geneon). Telomere region was amplified with primers Tel1 (GGTTTTTGAGGGTGAGGG TGAGGGTGAGGGTGAGGGTGAGGGT) and Tel2 (TCCCGACTAT CCCTATCCCTATCCCTATCCCTATCCCTATCCCTA), while a single-copy reference gene (36B4) was amplified with primers 36B4F (CAG-CAAGTGGGAAGGTGTAATCC) and 36B4R (CCCATTCTATCAT-CAACGGGTACAA) for normalization. qPCR was performed with the following cycling conditions: 95 °C for 5 min, followed by 40 cycles of 95 °C for 30 s and 60 °C for 30 s, and 72 °C for 1 min. Relative telomere length was calculated using the $2^{-\Delta\Delta Ct}$ method. All experiments were repeated four times.

Comet assay

The alkaline comet assay was performed using a comet assay kit (Abbkine, China). LS174T and HCT116 cells were treated with DMSO, ZBH-01, SN-38, CPT-11, and TMPyP4 for 48 or 72 h. Cells were resuspended in low-melting-point agarose and layered onto Comet Slides. The slides were immersed in lysis solution and incubated at 4 °C for 2 h in the dark. After lysis, the solution was discarded, and slides were treated with alkaline deconvolution solution in the dark at 4 °C for 2 h. Electrophoresis was performed in alkaline electrophoresis buffer. The slide was then immersed in 0.4 mM Tris-HCl buffer (pH 7.5) and neutralized three times (10 min each). After removing the buffer, slides were stained with propidium iodide (PI). Comet tails were visualized using confocal microscopy and analyzed with ImageJ using the OpenComet plugin.

Colony formation assay

LS174T, HCT116 or SW480 cells were seeded in 6-well plates (1000–2000 cells/well) and treated with DMSO, ZBH-01, SN-38, CPT-11, TMPyP4 or the combination of CPT-11 and TMPyP4, SN-38 and TMPyP4 for 11 days. After removing the medium, cells were fixed with methanol for 15 min. The methanol was discarded, and colonies were stained with 1% crystal violet for 15 min. Following PBS washes, colonies were photographed and quantified for analysis. Experiments were performed in triplicate.

Senescence β-galactosidase (SA-β-Gal) assay

Cellular senescence was detected using a β-galactosidase staining kit (Solarbio). LS174T and SW480 cells were seeded in a 6-well plate and treated with DMSO, ZBH-01, SN-38, CPT-11, TMPyP4 or the combination of CPT-11 and TMPyP4, SN-38 and TMPyP4 for 2 or 5 days. After removing the medium, cells were washed once with PBS and fixed with 1 mL β-gal fixative for 15 min at room temperature. The fixative was discarded, and cells were washed three times with PBS. Staining solution (1 mL) was added to each well, and plates were incubated at 37 °C for 16 h. Senescent cells were visualized under a light microscope.

Statistics and reproducibility

Statistical analyses were performed using GraphPad Prism 9 (GraphPad Software Inc., La Jolla, CA, RRID: SCR_002798). For comparisons between independent experimental groups (e.g., ligand-treated vs. control cells), two-tailed unpaired Student's *t*-test analysis was used to assess bidirectional differences without pre-assuming directionality. Survival analysis was performed using the Kaplan-Meier method. Data were summarized as mean ± standard deviation (SD) or standard error of the mean (SEM) for at least three independent experiments. A $p < 0.05$ was considered statistically significant.

Reporting summary

Further information on research design is available in the Nature Portfolio Reporting Summary linked to this article.

Data availability

The data that support this study are available from the corresponding authors upon reasonable request. All protocols used in this study are available in the "Methods" sections. All RNA-seq data generated in this study are deposited in the NCBI Sequence Read Archive (SRA) database under BioProject accession code PRJNA1387424 and in the Gene Expression Omnibus (GEO) database under accession code GSE314702. The structure coordinate data for the *hTERT* G4s in complex with CPT-11 or ZBH-01 generated in this study have been deposited in the Protein Data Bank under PDB accession code 9VA0 and 9VA3. The NMR data are deposited in the Biological Magnetic Resonance Data Bank (BMRB code 36761). The source data underlying the graphs in this paper are provided with the paper and can be found in the Supplementary Data. Supplementary Information is available in the online version of the paper.

Received: 18 June 2025; Accepted: 23 February 2026;
Published online: 09 March 2026

References

1. Roelands, J. et al. An integrated tumor, immune and microbiome atlas of colon cancer. *Nat. Med.* **29**, 1273–1286 (2023).
2. Lancet, T. GLOBOCAN 2018: counting the toll of cancer. *Lancet* **392**, 985 (2018).
3. Berian, J. R., Benson, A. B. III. & Nelson, H. Young age and aggressive treatment in colon cancer. *J. Am. Med. Assoc.* **314**, 613–614 (2015).
4. Willyard, C. The colon cancer conundrum. *Nature* https://doi.org/10.1038/d41586-021-03405-6 (2021).
5. Liu, C., Banister, C. E. & Buckhaults, P. J. Spindle assembly checkpoint inhibition can resensitize p53-null stem cells to cancer chemotherapy. *Cancer Res.* **79**, 2392–2403 (2019).
6. Hamamoto, Y. et al. A phase I/II study of XELIRI plus bevacizumab as second-line chemotherapy for Japanese patients with metastatic colorectal cancer. *Oncologist* **19**, 1131–1132 (2014).
7. Lu, W. et al. Effect of reduced-dose capecitabine plus cetuximab as maintenance therapy for RAS wild-type metastatic colorectal cancer: a phase 2 clinical trial. *JAMA Netw. open* **3**, e2011036 (2020).
8. Luput, L. et al. Liposomal simvastatin sensitizes C26 murine colon carcinoma to the antitumor effects of liposomal 5-fluorouracil in vivo. *Cancer Sci.* **111**, 1344–1356 (2020).
9. Shi, Z. et al. Targeting HNRNPU to overcome cisplatin resistance in bladder cancer. *Mol. Cancer* **21**, 37 (2022).
10. Park, S. H. et al. Sonic hedgehog pathway activation is associated with cetuximab resistance and EPHB3 receptor induction in colorectal cancer. *Theranostics* **9**, 2235–2251 (2019).
11. Gongora, C. et al. New Topoisomerase I mutations are associated with resistance to camptothecin. *Mol. Cancer* **10**, 64 (2011).
12. Coussy, F. et al. BRCAness, SLFN11, and RB1 loss predict response to topoisomerase I inhibitors in triple-negative breast cancers. *Sci. Transl. Med.* **12**, eaax2625 (2020).
13. Wang, W. et al. Tyrosyl-DNA phosphodiesterase 1 and topoisomerase I activities as predictive indicators for Glioblastoma susceptibility to genotoxic agents. *Cancers* **11**, 1416 (2019).
14. Jingjing, L. et al. Nanoparticle-enhanced chemo-immunotherapy to trigger robust antitumor immunity. *Sci. Adv.* **6**, eabc3646 (2020).
15. Jameson, G. et al. A multicenter, phase I, dose-escalation study to assess the safety, tolerability, and pharmacokinetics of etirinotecan

pegol in patients with refractory solid tumors. *Clin. Cancer Res.* **19**, 268–278 (2013).
16. Lee, B. et al. A novel mechanism of irinotecan targeting MDM2 and Bcl-xL. *Biochem. Biophys. Res. Commun.* **514**, 518–523 (2019).
17. Innocenti, F. et al. Comprehensive pharmacogenetic analysis of irinotecan neutropenia and pharmacokinetics(Article). *J. Clin. Oncol.* **27**, 2604–2614 (2009).
18. Si, J., Zhao, X., Gao, S., Huang, D. & Sui, M. Advances in delivery of Irinotecan (CPT-11) active metabolite 7-ethyl-10-hydroxycamptothecin. *Int. J. Pharm.* **568**, 118499 (2019).
19. Senter, P. D., Beam, K. S., Mixan, B. & Wahl, A. F. Identification and activities of human carboxylesterases for the activation of CPT-11, a clinically approved anticancer drug. *Bioconjugate Chem.* **12**, 1074–1080 (2001).
20. Satoh, T. et al. Metabolic activation of CPT-11, 7-ethyl-10-[4-(1-piperidino)-1- piperidino]carbonyloxycamptothecin, a novel antitumor agent, by carboxylesterase. *Biol. Pharm. Bull.* **17**, 662–664 (1994).
21. Yang, D. G-Quadruplex DNA and RNA. *Methods Mol. Biol.* **2035**, 1–24 (2019).
22. Todd, A. K., Johnston, M. & Neidle, S. Highly prevalent putative quadruplex sequence motifs in human DNA. *Nucleic Acids Res.* **33**, 2901–2907 (2005).
23. Rauchhaus, J., Robinson, J. & Monti, L. G-quadruplexes mark sites of methylation instability associated with ageing and cancer. *Genes* **13**, 1665 (2022).
24. Teng, F. et al. G-quadruplex DNA: a novel target for drug design. *Cell. Mol. Life Sci.* **78**, 6557–6583 (2021).
25. Yang, Q.-F. et al. G4LDB 3.0: a database for discovering and studying G-quadruplex and i-motif ligands. *Nucleic Acids Res.* **53**, 91–98 (2025).
26. Tian, T., Chen, Y., Wang, S. & Zhou, X. G-Quadruplex: a regulator of gene expression and its chemical targeting. *Chem* **4**, 1314–1344 (2018).
27. Andreasson, M. et al. Exploring the dispersion and electrostatic components in arene–arene interactions between ligands and G4 DNA to develop G4-ligands. *J. Med. Chem.* **67**, 2202–2219 (2024).
28. Liu, T. et al. RBFOX3 promotes tumor growth and progression via hTERT signaling and predicts a poor prognosis in hepatocellular carcinoma. *Theranostics* **7**, 3138–3154 (2017).
29. Cohen, S. B. et al. Protein composition of catalytically active human telomerase from immortal cells. *Sci* **315**, 1850–1853 (2007).
30. Lim, K. W. et al. Coexistence of two distinct G-quadruplex conformations in the hTERT promoter. *J. Am. Chem. Soc.* **132**, 12331–12342 (2010).
31. Monsen, R. C. et al. The hTERT core promoter forms three parallel G-quadruplexes. *Nucleic Acids Res.* **48**, 5720–5734 (2020).
32. Wei, L. et al. Targeting hTERT promoter G-quadruplex DNA structures with small-molecule ligand to downregulate hTERT expression for triple-negative breast cancer therapy. *J. Med. Chem.* **67**, 13363–13382 (2024).
33. Wheelhouse, R. T., Sun, D., Han, H., Han, F. X. & Hurley, L. H. Cationic porphyrins as telomerase inhibitors: the interaction of tetra-(N-methyl-4-pyridyl)porphine with quadruplex DNA. *J. Am. Chem. Soc.* **120**, 3261–3262 (1998).
34. Zhou, M., He, X., Shi, W. & Zhong, B. Synthesis and preliminary evaluation of novel 10-substituted 7-ethyl-10-hydroxy camptothecin(SN38) prodrugs. *Chin. J. Med. Chem.* **24**, 337–344 (2014).
35. Yang, X.-Y. et al. Synthesis and biological evaluation of 10-substituted camptothecin derivatives with improved water solubility and activity. *ChemMed Chem.* **16**, 1000–1010 (2021).
36. Barretina, J. et al. The Cancer Cell Line Encyclopedia enables predictive modelling of anticancer drug sensitivity. *Nat* **491**, 603–607 (2012).
37. Staker, B. L. et al. Structures of three classes of anticancer agents bound to the human topoisomerase I-DNA covalent complex. *J. Med. Chem.* **48**, 2336–2345 (2005).
38. Zhang, S., Tischer, T. & Barford, D. Cyclin A2 degradation during the spindle assembly checkpoint requires multiple binding modes to the APC/C. *Nat. Commun.* **10**, 1–16 (2019).
39. Monsen, R. C., Maguire, J. M., DeLeeuw, L. W., Chaires, J. B. & Trent, J. O. Drug discovery of small molecules targeting the higher-order hTERT promoter G-quadruplex. *PLoS One* **17**, 1–25 (2022).
40. Dickerhoff, J., Dai, J. & Yang, D. Structural recognition of the MYC promoter G-quadruplex by a quinoline derivative: insights into molecular targeting of parallel G-quadruplexes. *Nucleic Acids Res.* **49**, 5905–5915 (2021).
41. Cogoi, S., Paramasivam, M. & Spolaore, B. Structural polymorphism within a regulatory element of the human KRAS promoter: formation of G4-DNA recognized by nuclear proteins. *Nucleic Acids Res.* **36**, 3765–3780 (2008).
42. Hsu, S. T. D. et al. A G-rich sequence within the c-kit oncogene promoter forms a parallel G-quadruplex having asymmetric G-tetrad dynamics. *J. Am. Chem. Soc.* **131**, 13399 (2009).
43. Ou, A. et al. High resolution crystal structure of a KRAS promoter G-quadruplex reveals a dimer with extensive poly-A π-stacking interactions for small-molecule recognition. *Nucleic Acids Res.* **48**, 5766–5776 (2020).
44. Wang, K.-B. et al. Indenoisoquinoline topoisomerase inhibitors strongly bind and stabilize the MYC promoter G-quadruplex and downregulate MYC. *J. Am. Chem. Soc.* **141**, 11059–11070 (2019).
45. Dai, J. et al. An intramolecular G-quadruplex structure with mixed parallel/antiparallel G-strands formed in the human BCL-2 promoter region in solution. *J. Am. Chem. Soc.* **128**, 1096–1098 (2006).
46. Sengar, A. et al. Structure of a (3+1) hybrid G-quadruplex in the PARP1 promoter. *Nucleic Acids Res.* **47**, 1564–1572 (2019).
47. Agrawal, P., Hatzakis, E., Guo, K., Carver, M. & Yang, D. Solution structure of the major G-quadruplex formed in the human VEGF promoter in K+: insights into loop interactions of the parallel G-quadruplexes. *Nucleic Acids Res.* **41**, 10584–10592 (2013).
48. Liu, W. et al. Structures of 1:1 and 2:1 complexes of BMVC and MYC promoter G-quadruplex reveal a mechanism of ligand conformation adjustment for G4-recognition. *Nucleic Acids Res.* **47**, 11931–11942 (2019).
49. Cheng, F. et al. DYT6 mutated THAP1 is a cell type dependent regulator of the SP1 family. *Brain* **145**, awac001 (2022).
50. Kyo, S. et al. Sp1 cooperates with c-Myc to activate transcription of the human telomerase reverse transcriptase gene (hTERT). *Nucleic Acids Res.* **28**, 669–677 (2000).
51. Das, S. K. et al. MYC assembles and stimulates topoisomerases 1 and 2 in a "topoisome. *Mol. Cell* **82**, 140 (2022).
52. He, L. et al. Wnt pathway is involved in 5-FU drug resistance of colorectal cancer cells. *Exp. Mol. Med.* **50**, 101 (2018).
53. Moraca, F. et al. Repurposing FDA-approved drugs to target G-quadruplexes in breast cancer. *Eur. J. Med. Chem.* **285**, 117245 (2025).
54. GCC, K. et al. The chemotherapeutic drug CX-5461 is a potent mutagen in cultured human cells. *Nat. Genet.* **56**, 23–26 (2024).
55. Drygin, D. et al. Anticancer activity of CX-3543: a direct inhibitor of rRNA biogenesis. *Cancer Res.* **69**, 7653–7661 (2009).
56. Xu, D., Gruber, A., Björkholm, M., Peterson, C. & Pisa, P. Suppression of telomerase reverse transcriptase (hTERT) expression in differentiated HL-60 cells: regulatory mechanisms. *Br. J. Cancer* **80**, 1156–1161 (1999).
57. Huang, Y. et al. Polo-like kinase 1 (Plk1) up-regulates telomerase activity by affecting human telomerase reverse transcriptase (hTERT) stability. *J. Biol. Chem.* **290**, 18865–18873 (2015).

58. Hou, M., Xu, D., Björkholm, M. & Gruber, A. Real-time quantitative telomeric repeat amplification protocol assay for the detection of telomerase activity. *Clin. Chem.* **47**, 519–524 (2001).
59. Chou, T.-C. Drug combination studies and their synergy quantification using the Chou-Talalay method. *Cancer Res.* **70**, 440–446 (2010).
60. Delaglio, F. et al. NMRPipe: a multidimensional spectral processing system based on UNIX pipes. *J. Biomol. NMR* **6**, 277–293 (1995).
61. Johnson, B. A. & Blevins, R. A. NMRView: a computer program for the visualization and analysis of NMR data. *J. Biomol. NMR* **4**, 603–614 (1994).
62. Br, A. T. et al. Crystallography & NMR system: a new software suite for macromolecular structure determination. *Acta Crystallogr. Sect. D. Biol. Crystallogr.* **54**, 905–921 (1998).
63. Rieping, W. et al. ARIA2: Automated NOE assignment and data integration in NMR structure calculation. *Bioinformatics* **23**, 381–382 (2007).

Acknowledgements

We thank the State Key Laboratory of Supramolecular Structure and Materials at Jilin University for the use of their research facilities. We acknowledge the BGI Group for generating RNA-seq data. We thank Di Liu for the assistance with ITC and NMR experiments, and Naicui Zhai for mass spectrometric analysis, both conducted in the core facility of the First Hospital of Jilin University. This work was supported in part by the research fund from the First Hospital of Jilin University (Changchun, China), International Center of Future Science, JLU, and National Natural Science Foundation of China (82372736; L.Z.).

Author contributions

Yameng Li performed experiments, Yingying Liang and Yongqi Li performed confocal microscopy observations and analyses, Yameng Li and Enwei Wei performed ChIP experiments, Yameng Li, Liping Wang and Chunfeng Gao performed cell experiments, Yameng Li, Donglei Ji, Zhen Guo and Yiqun Zhang analyzed sequencing data, Yameng Li, Yanjie Jia, Chunyu Wang and Lei Zeng collected and analyzed NMR data, Yameng Li and Lei Zeng wrote the manuscript with input from all co-authors. Di Wu, Caroline Zeng, and Ming-Ming Zhou revised the manuscript.

Competing interests

The authors declare no competing interests.

Additional information

Supplementary information The online version contains supplementary material available at https://doi.org/10.1038/s42003-026-09801-w.

Correspondence and requests for materials should be addressed to Ming-Ming Zhou, Di Wu or Lei Zeng.

Peer review information *Communications Biology* thanks the anonymous reviewers for their contribution to the peer review of this work. Primary Handling Editors: Luciano Abriata, George Inglis and Mengtan Xing.